

Subvortices within a Numerically Simulated Tornado: The Role of Unstable Vortex Rossby Waves

WEI HUANG^a AND MING XUE^{b,c}

^a Key Laboratory of Mesoscale Severe Weather, Ministry of Education, School of Atmospheric Sciences, Nanjing University, Nanjing, Jiangsu, China

^b Center for Analysis and Prediction of Storms, University of Oklahoma, Norman, Oklahoma

^c School of Meteorology, University of Oklahoma, Norman, Oklahoma

(Manuscript received 13 November 2022, in final form 25 July 2023, accepted 27 July 2023)

ABSTRACT: Multiple subvortices corresponding to suction vortices in observations are obtained within a simulated tornado for the EF4 tornado case of Funing, China, on 23 June 2016. Within the simulation, the tornado evolves from a one-cell structure with vorticity maximum at its center to a two-cell structure with a ring of vorticity maximum. Five well-defined subvortices develop along the ring. The radial profile of tangential wind across the vorticity ring satisfies the necessary condition of barotropic instability associated with phase-locked, counterpropagating vortex Rossby waves (VRWs) along the ring edges. The phased-locked waves revolve around the parent vortex at a speed less than the maximum azimuthal-mean tangential velocity, agreeing with theoretically predicted VRW phase speed. The radii within which the wave activities are confined are also correctly predicted by the VRW theory where radial group velocity approaches zero. Several other characteristics related to the simulated subvortices agree with VRW theories also. The most unstable azimuthal wavenumber depends on the width and the relative magnitude of vorticity of the vortex ring. Their values estimated from the simulation prior to subvortex formation correctly predict wavenumber 5 as the most unstable. The largest contribution to wave kinetic energy is diagnosed to be from the radial shear of azimuthal wind term, consistent with barotropic instability. Vorticity diagnostics show that vertical vorticity stretching is the primary vorticity source for the intensification and maintenance of the simulated subvortices.

SIGNIFICANCE STATEMENT: Multiple subvortices or suction vortices in tornadoes can produce extreme damage but their cause is not well understood. An intense tornado from China that developed five strong subvortices, along a vorticity ring a distance from the tornado vortex center, was successfully simulated. By examining the propagation and other characteristics of these subvortices and comparing them with theoretical models of vortex Rossby waves (VRWs) that have been studied mostly in the context of typhoons/hurricanes, it is believed that nonlinear growth of unstable VRWs associated with barotropic instability is the primary reason for the development of subvortices within the tornado. The conclusion is further supported by analyses of the primary source of wave growth energy. Vertical vorticity stretching is the main vorticity source for intensifying and maintaining the subvortices at their development and mature stages. The unstable growth of VRWs as the cause of tornado suction vortices has not been analyzed in detail for realistic tornadoes until now.

KEYWORDS: Tornado genesis; Wave properties; Atmospheric waves; Vorticity

1. Introduction

During their mature stage, tornadoes sometimes undergo a significant change from a one-cell to two-cell structure and further evolve from a single tornado vortex to one that contains multiple subvortices (Davies-Jones 1986). These multivortices are also known as suction vortices because of the damage patterns they produce on the ground (Fujita et al. 1976). Such suction vortices have been visually observed and verified by ground damage surveys since early days of tornado studies (Fujita 1970, 1972; Ward 1972; Fujita et al. 1976; Snow 1978; Fujita 1981) and later in high-resolution mobile Doppler radar observations (Wurman 2002; Alexander and Wurman 2005; Bluestein et al. 2003; Lee and Wurman 2005; Kosiba and Wurman 2010). The suction vortices can produce very local, extreme damages due to the superposition

of their intense circulations with the parent tornado vortex circulation.

The multivortices within tornado have been explored in experiments with laboratory chambers (Ward 1972; Church et al. 1977, 1979), and in numerical simulations of tornado chamber configurations (Rotunno 1984; Fiedler 1998, 2009; Nolan 2012) that often employ large-eddy simulation (LES) resolutions (Lewellen et al. 1997; Lewellen et al. 2000; Lewellen and Lewellen 2007a,b; Bryan et al. 2017; Nolan et al. 2017). Snow (1978) suggested that inertial instability is the mechanism to initiate the multiple subvortices. Rotunno (1978) found that the multivortices are related to the instability on a cylindrical vortex sheet. The radial shear of azimuthal wind and radial shear of mean vertical velocity are the main sources of instability energy. As the swirl ratio increases, the effect of radial shear on mean vertical velocity becomes more important.

Barotropic instability, also known as horizontal shear instability (Markowski and Richardson 2010), has also been studied for a circular vortex flow (e.g., Michalke and Timme 1967). A

Corresponding author: Ming Xue, mxue@ou.edu

DOI: 10.1175/JAS-D-22-0237.1

© 2023 American Meteorological Society. This published article is licensed under the terms of the default AMS reuse license. For information regarding reuse of this content and general copyright information, consult the AMS Copyright Policy (www.ametsoc.org/PUBSReuseLicenses).

few studies (Staley and Gall 1979; Gall 1983; Walko and Gall 1984; Lee and Wurman 2005) have suggested barotropic instability as a possible mechanism of multivortex formation in tornadoes, although few performed detailed analyses on the mechanism, at least in the context of tornado multivortices. Staley and Gall (1979) studied an idealized vortex with a core of constant angular velocity and constant vorticity surrounded by a vorticity ring containing twice as large vorticity and found that barotropic instability may lead to the formation of multiple vortices. Based on Staley and Gall (1979), Gall (1983) further explored the energy source of barotropic instability through an axisymmetric model and proposed that there are two modes of barotropic instability that can result in multiple vortices. One mode appears at higher swirl ratios and the most unstable wavenumber is above 4, and the vortices receive most energy from the radial shear of tangential wind. The second mode occurs with lower swirl ratios and only exists in wavenumbers 1 and 2, and receives most energy from the radial shear of vertical velocity. The results were substantiated by Walko and Gall (1984) through idealized simulations with a three-dimensional model. Lee and Wurman (2005) observed a train of quasi-periodic subvortices in a tornado and found the existence of vortex rings through the ground-based velocity track display (GBVTD) technique. They speculated that the reversal in the sign of radial gradient of vertical vorticity immediately inside and outside the vorticity ring, which meets the Rayleigh necessary condition of barotropic instability, could have caused the growth of perturbations on the parent vortex and generation of the multivortex structure. Terwey and Montgomery used their data to perform a linear barotropic stability analysis and obtained wavenumber-2 and -3 instabilities (presented at a conference, M. Montgomery 2023, personal communication).

The structure of polygonal eyewall and subvortices have also been found in hurricanes, which are believed to be due to barotropic instability (Kuo et al. 1999; Kossin and Schubert 2001; Kossin et al. 2002; Kossin and Schubert 2004; Rozoff et al. 2006; Hendricks et al. 2012). At the mature stage, hurricanes exhibit a ring of enhanced PV in the eyewall region, characterized by radial vorticity gradients of opposite signs at the inner and outer edges of the eyewall. Schubert et al. (1999) found that such a vorticity structure supports counterpropagating vortex Rossby waves (VRWs) on the two edges of vorticity ring that are locked in phase and cause barotropic instability. The VRWs that develop along the sharp edges of enhanced vorticity ring are often called discrete VRWs (Reasor et al. 2000). In idealized barotropic vortex models studied in Snow (1978), a top-hat radial velocity profile has been assumed, where the radial gradient of vorticity changes sign across the “hat” or vorticity ring; waves developing and propagating along the edges have been called “vortex Rossby edge waves” (e.g., Reasor et al. 2000). The gradient of vorticity provides a state on which Rossby waves can propagate, as they do on Earth with the β effect. Due to the different signs of gradient, VRWs on the outer edge of the vorticity ring would propagate slower than (retrograde) the azimuthal mean tangential flow, while the VRWs on the inner edge of the ring would propagate faster than (prograde) the mean tangential flow. These two trains of VRWs can be locked in phase, causing exponential growth of the waves, i.e., barotropic

instability (Schubert et al. 1999; Terwey and Montgomery 2002). As the waves grow, the vorticity pools into a small number of vorticity pockets, and isolated subvortices can form (Schubert et al. 1999; Kuo et al. 1999; Hendricks et al. 2009), similar to the cutoff lows associated with planetary Rossby waves in the polar vortex. Terwey and Montgomery (2002) generalized the top-hat vorticity profile used in Schubert et al. (1999) so that wavenumber 2 could be unstable. Kuo et al. (1999), also using the top-hat profile, the elliptical eye found in their idealized simulations was associated with wavenumber-2 discrete VRWs. Reasor et al. (2000) attributed asymmetries of hurricane inner-core region to a wavenumber-2 discrete vortex Rossby edge waves. Muramatsu (1986) surmised that the formation mechanism of polygonal eyewalls may be similar to that of subvortices within tornadoes due to barotropic instability.

VRWs can also exist outside the vorticity ring where vorticity generally decreases more smoothly with radius. In such a region, the VRWs would be continuously sheared by the radially decreasing azimuthal flow and appear as spiral bands. Apart from the apparent outward propagation related to the spiral pattern, there is also outward propagation of wave energy of the VRWs that become stagnant at the radius where group velocity becomes zero (Montgomery and Kallenbach 1997). This group of VRWs is often called sheared VRWs and is linked to spiral rainbands, tropical cyclogenesis, and secondary eyewall formation in hurricanes (Guinn and Schubert 1993; Möller and Montgomery 1999, 2000; Wang 2002; Qiu et al. 2010; Hall et al. 2013).

Although the subvortices in tornadoes have been observed for a long time, so far most insights on their possible formation mechanisms have mainly been gained through idealized analytical models or highly idealized vortex simulations (Rotunno 1977, 1979, 1984; Fiedler 1994, 1995, 1998, 2009; Nolan 2012; Rotunno et al. 2016). Detailed investigations based on realistic simulations of tornadoes that occur within real storms do not yet exist, according to our knowledge. The multiple subvortices in realistic tornadoes need at least ~ 50 m grid spacing to resolve (Xue et al. 2014; Mashiko and Niino 2017; Sun et al. 2019). Xue et al. (2014) successfully simulated the life cycle of a tornado that occurred in the 8 May 2003 Oklahoma City supercell storm, using a nested 50 m grid. The simulated tornado went through two cycles of one-cell, two-cell, then multivortex structures. For a supercell storm that occurred on 6 May 2012 in Tsukuba, Japan, Mashiko and Niino (2017) also simulated the evolution from one-cell to two-cell vortex, and subsequently to four subvortices with a horizontal grid spacing of 10 m. In a realistic simulation for an EF4 tornado that occurred on 23 June 2016, in Funing, Jiangsu Province, China (Meng et al. 2018), Sun et al. (2019) documented the development of five well-defined subvortices that developed along a vorticity ring within a tornado vortex, using 49 m grid spacing. Although these studies simulated multiple tornado subvortices in real storms, the mechanism of the subvortex formation was not analyzed in detail; at most the possible causes were speculated on. Therefore, detailed studies on the primary mechanism of subvortices in tornadoes, especially in realistic ones, are still needed.

The existence of multiple subvortices within the EF4 Funing tornado was also suggested by Meng et al. (2018) based

on damage surveys. The irregular strong wind swaths in the simulation of Sun et al. (2019) are consistent with certain damage paths observed by Meng et al. (2018). In our study, we analyze the simulation of Sun et al. (2019) and investigate the formation mechanism of the subvortices in the simulated tornado. Specifically, this paper addresses the following questions: What is the primary mechanism for the formation of the subvortices within the tornado vortex? Why there are five subvortices at their fully developed stage? What parameters affect the subvortex structures? What is the primary energy source for wave growth? What process is primarily responsible for the production of strong vertical vorticity that intensifies and maintains the subvortices?

The remainder of this paper is organized as follows. In section 2, we provide an overview of the Funing tornado case and introduce the simulation results to be analyzed. Section 3 describes the characteristics and evolution of five subvortices that develop on a vorticity ring in the simulated tornado. Section 4 discusses dispersion relations of VRWs in 2D barotropic models, and examines their agreements with model-simulated waves. Section 5 examines the most unstable wavenumber based on two parameters of the idealized parent vortex proposed by Schubert et al. (1999), and suggests that unstable growth of VRWs due to barotropic instability is the cause of nonlinear development of the subvortices. In section 6, we conduct an analysis of the source terms of wave kinetic energy growth within the simulated data, and confirm that barotropic instability is the main mechanism for wave amplification. In section 7, the source/sink terms of vertical vorticity of the subvortices are diagnosed to identify the main process responsible for subvortex vorticity intensification and maintenance. A summary is given in section 8.

2. Numerical simulation of the Funing tornado

The tornado of interest occurred in Funing County of Yangcheng City, in northern Jiangsu Province, China, in the afternoon of 23 June 2016. The tornado formed at approximately 0615 UTC (1415 LST) and dissipated at 0700 UTC (1500 LST). It was the deadliest tornado in the past 40 years in China and caused 98 fatalities. It produced a swath of EF1–EF4 rated damages of about 35 km long and up to 4.1 km wide (Meng et al. 2018). Due to heavy precipitation wrapping, no photograph of the tornado funnel was available, although videos of rotating air flows and flying debris were recorded. The synoptic background of the case has been documented in several studies (Xue et al. 2016; Meng et al. 2018; Sun et al. 2019) so only a brief introduction is given here.

The Funing tornado was spawned by a supercell storm that developed south of a mei-yu frontal rainband and ahead of a deep 500 hPa trough extending from a cold vortex in northeast China. At the 850 hPa level, an inverted trough extended from the Sichuan Province in southwest China through Shandong Province north of Jiangsu and strong southwesterly flows between the trough and the western Pacific subtropical high brought warm moist air from the South China Sea to northern Jiangsu Province (not shown). Based on a sounding taken at 0600 UTC 60 km east of the tornadic storm, the

maximum unstable convective available potential energy (MUCAPE) was 2663 J kg^{-1} with a small CIN of 8 J kg^{-1} .

Sun et al. (2019) simulated the Funing tornado using the WRF-ARW Model (Skamarock et al. 2008) with five levels of nested grids. The horizontal grid spacings of the nests are 4000, 1333, 444, 148, and 49 m, integrated using time steps of 25, 8.33, 2.78, 0.93, and 0.31 s, respectively. The innermost domain is $117 \text{ km} \times 94 \text{ km}$, which can cover most of the tornado life cycle. All domains have 51 vertical levels. The vertical grid is stretched with the lowest model level above ground being 10 m. The three outermost nests are initialized at 23 June 2016 using the NCEP GFS 0000 UTC analysis and run in a two-way interactive mode, and the fourth and fifth nested grids are spawn at 0435 and 0500 UTC, respectively, to provide additional resolution over the tornadic storm. The innermost domain uses the fully three-dimensional 1.5-order turbulent kinetic energy (TKE)-based subgrid-scale (SGS) turbulence closure scheme based on Deardorff (1974) and the other four grids use the Smagorinsky deformation-based horizontal SGS turbulence mixing parameterization (Smagorinsky 1963). The Pleim–Xiu land surface and surface layer models (Pleim 2006) coupled with the Asymmetric Convective Model (version 2, ACM2) PBL scheme (Pleim 2007) are used on all grids. Surface drag (or momentum flux) that is believed to be important for tornado dynamics according to recent studies (e.g., Schenkman et al. 2014; Roberts et al. 2016, 2020; Roberts and Xue 2017; Tao and Tamura 2020) are calculated by the surface physics scheme based on local surface roughness conditions (the tornadic region is mostly flat farmland) and stability. The roughness length in the region of the tornado storm is about 0.1–0.8 m. The two-moment Morrison microphysics scheme (Morrison and Grabowski 2008) is used without cumulus parameterization on all grids. More details on the model configuration and design of experiments can be found in section 4 of Sun et al. (2019).

The simulation produces the full life cycles of five subvortices within the tornado vortex on the innermost grid. The initially one-cell tornado structure evolves into a vorticity ring structure then into five subvortices, and eventually decay. The trochoidal paths of the vortices on the ground are consistent with damage survey indications (Meng et al. 2018) where irregular damage paths are similar to those observed by Fujita and Grandoso (1968). These subvortices in the 49 m simulation create localized regions of intense winds exceeding 60 m s^{-1} at the lowest model level ($\sim 26 \text{ m}$) above ground. There are timing and location errors with the simulation though, compared to observation. The Funing tornado substantially strengthened after 0700 UTC in the simulation, while in observations, it reached EF4 intensity at 0630 UTC (details can be found in Sun et al. 2019). The Funing tornado in the simulation is displaced northward compared to the observation [refer to Fig. 15 in Meng et al. (2018) and Fig. 11 in Sun et al. (2019)]. Since our focus is on the formation mechanism of the subvortices, the timing and location errors are acceptable.

Figure 1 shows the horizontal and vertical cross sections of vertical vorticity ζ and horizontal wind vectors associated with the most intense tornado simulated on the 49 m grid at 0716 and 0724 UTC. As described in Sun et al. (2019), the strength of

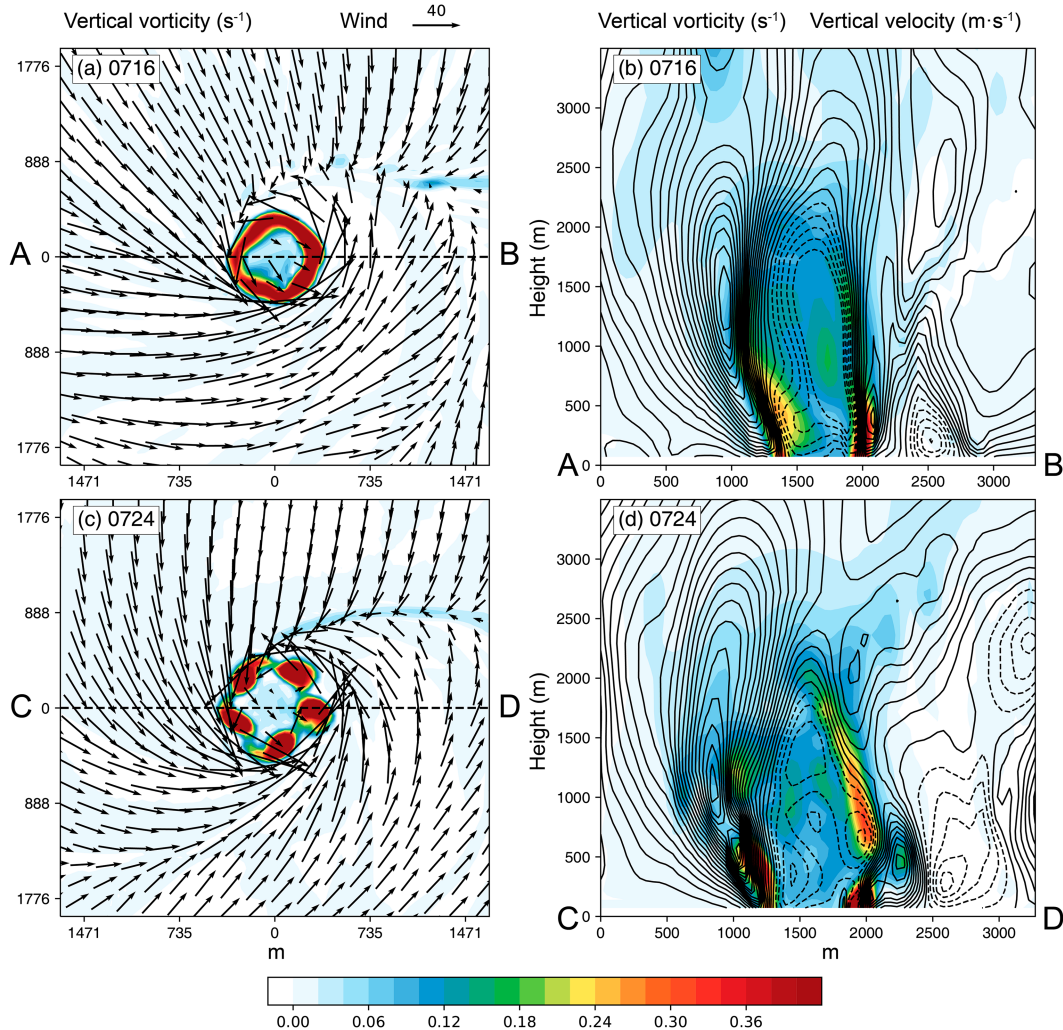


FIG. 1. (left) Vertical vorticity ζ (shaded; s^{-1}) and horizontal wind vectors at ~ 26 m AGL simulated by the 49 m grid at the vorticity ring and multivortex stages. (right) Vertical cross sections of vertical vorticity ζ (shaded; s^{-1}) and vertical velocity w (contours every 2 m s^{-1} with negative contours dashed). The location of the cross sections are marked as dashed lines in the left panels. The plotted times in UTC are shown in the figure (based on Fig. 8 of Sun et al. 2019).

the main tornado vortex changes rapidly during this period. About 20 min before 0716 UTC, the tornado has a “one-cell” structure (Davies-Jones et al. 2001) with vorticity maximum located at the vortex center (see Fig. 8a of Sun et al. 2019). By 0716 UTC, the one-cell structure has evolved into a well-defined “vorticity ring” structure (Fig. 1a), where the largest ζ is concentrated in a ring displaced from the vortex center. Some undulations on the mostly circular ring suggest that four to five waves are developing. The vertical cross section through the center of the vortex (Fig. 1b) indicates a pronounced “two-cell” (Davies-Jones et al. 2001) structure. Large ζ is displaced from the vortex center and large positive vertical velocity w is found outside the ring where the radial flow convergence is strongest. A downdraft occupies the vortex center below 2 km AGL inside of the vorticity ring. Between 0716 and 0724 UTC, five subvortices with distinct ζ maxima develop along the vorticity ring (Fig. 1c).

The subvortices are generally as deep as the original vortex ring in Fig. 1b (~ 700 m AGL). Within the subvortices (e.g., the one at $x = 2000$ m in Fig. 1d), enhanced positive and negative w coexist. The formation mechanism of these subvortices is the focus of this study.

The original output time interval of Sun et al. (2019) was 1 min, which is too coarse to even track the rapidly revolving subvortices within the parent vortex. For this study, the simulation is rerun with outputs every 3 s to allow for detailed analyses of the formation and maintenance mechanisms of the subvortices.

3. The evolution of subvortices

To examine the detailed evolution of the tornado vortex as well as the embedded subvortices described earlier, we show in Fig. 2 ζ and wind vectors at the first model level above

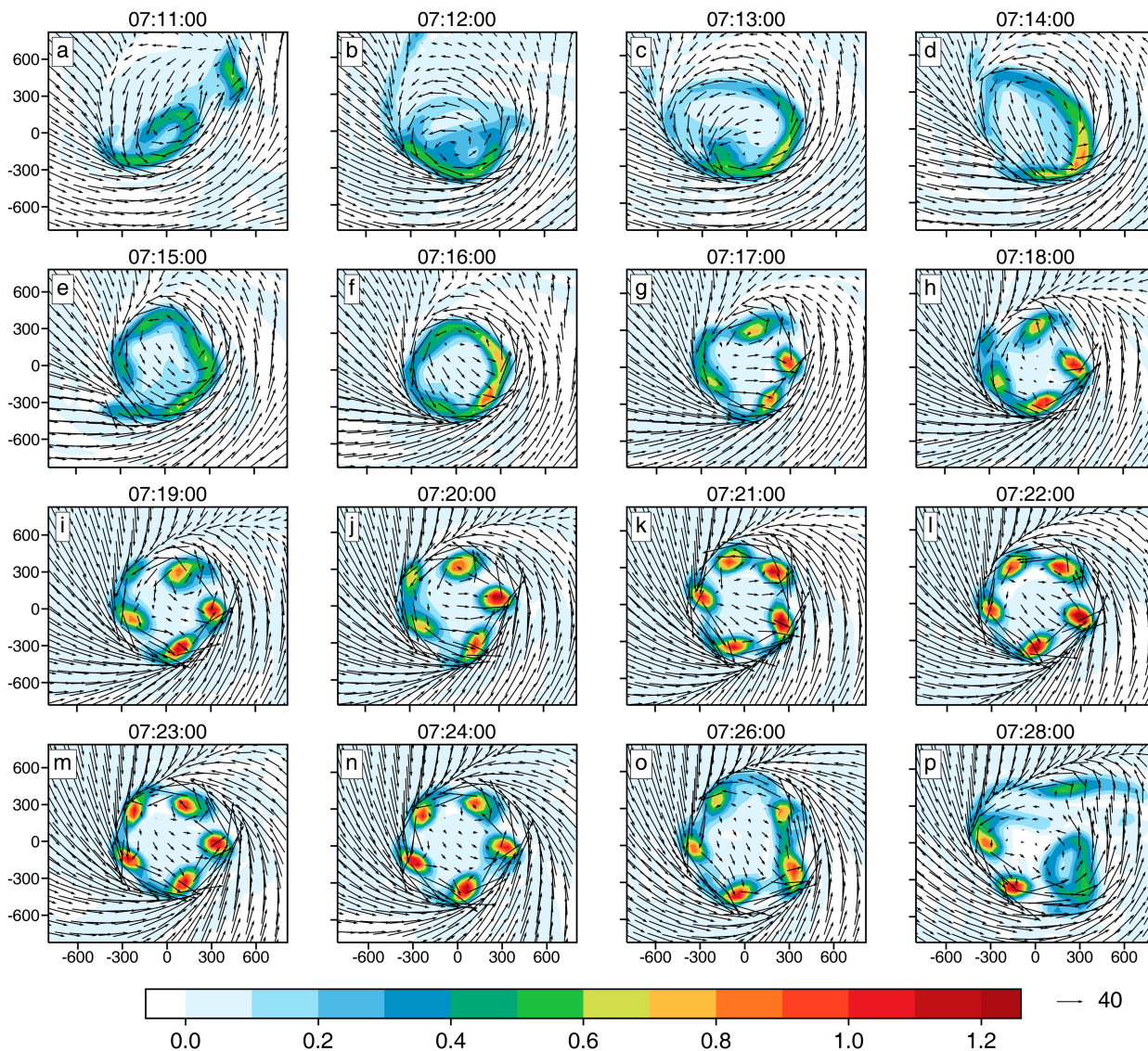


FIG. 2. ζ (shaded; s^{-1}) and horizontal wind vectors associated with the simulated tornado vortex at ~ 26 m AGL from 0711 to 0724 UTC and at 0726 and 0728 UTC. The coordinate origin is always defined at the center of the tornado vortex and the axes are in meters.

ground (~ 26 m) in a smaller domain following the tornado vortex, every 1 min from 0711 through 0724 UTC and every 2 min from 0724 through 0728 UTC to cover the life cycle of subvortices. The tornado vortex center is subjectively determined at different times. Hall et al. (2013) used an objective method to determine the center of a simulated typhoon. It is not applied here because the tornado vortex is very asymmetrical before 0715 UTC (Figs. 2a–d) and after five subvortices start to decay after 0726 UTC (Figs. 2o,p).

At 0655 UTC, maximum vorticity exists at the center of tornado vortex (cf. Fig. 8a of Sun et al. 2019), having a one-cell structure. From 0700 to 0706 UTC, a series of small vortices forming along a convergence zone with high ζ north of the tornado vortex revolve counterclockwise around the main tornado vortex and are drawn into the vortex by a strong near-

surface convergent flow toward the tornado vortex center. These small vortices are drawn into and absorbed one by one by the main vortex. By 0706 UTC, strong vorticity is organized into a semiclosed ring vortex (cf. Fig. 9 of Sun et al. 2019). The vortex ring remains unsteady and highly asymmetric, and is not completely closed until 0711 UTC (Fig. 2a) through 0714 UTC (Fig. 2d). By 0715 UTC, the vortex ring becomes almost closed (Fig. 2e), and becomes fully closed by 0716 UTC (Fig. 2f); 0716 UTC is also the time the vortex circulation has most axisymmetry and is sampled in Fig. 1a, but even at this time, the vorticity is not uniform across the vorticity ring. There are two vorticity maxima on the east side of the vorticity ring, and there are two weaker local maxima on the south-southeast, and north-northwest sides of the ring (Fig. 2f), suggesting that wavenumbers 1 and 4 would be the

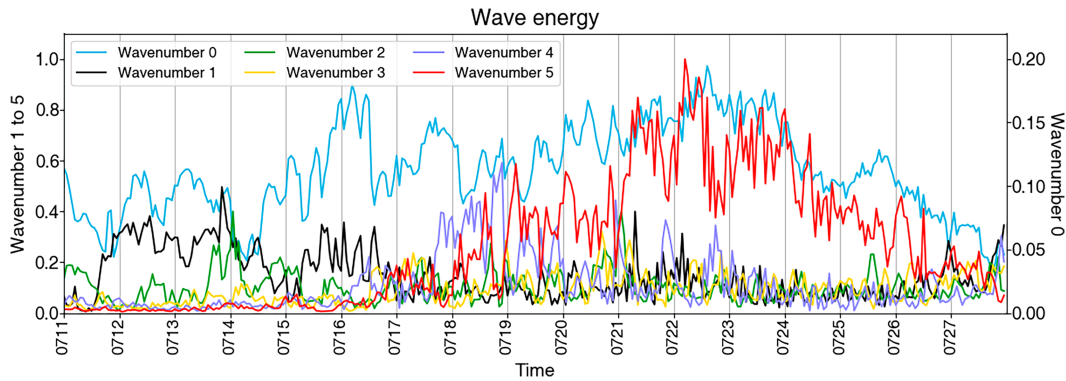


FIG. 3. Time series of wave energy (m^2s^{-2}) of ζ from 0711:00 to 0727:57 UTC at ~ 26 m AGL. The blue line represents the energy of wavenumber 0 corresponding to the axis label on the right. The black, green, yellow, purple, and red lines are for the energy of wavenumbers 1, 2, 3, 4, and 5, respectively.

dominant modes if one does Fourier decomposition along the azimuthal direction at this time.

Within the next minute, by 0717 UTC, the closed vorticity ring again breaks up, forming four vorticity maximum centers (Fig. 2g). The four maximum vorticity centers become well-defined quasi-circular vortex centers by 0718 UTC while a much weaker local vorticity maximum starts to establish at the northwest side of overall vortex (Fig. 2h). By 0720 UTC, this weaker maximum has gained intensity (Fig. 2j) and becomes one of the five subvortices that are sustained through 0726 UTC (Figs. 2j–o). The period from 0721 through 0724 UTC is when the five subvortices are the strongest. Afterward, they start to weaken (Figs. 2o,p). By 0728 UTC, one of five subvortices disappears and only two subvortices maintain their shapes of vortex, while the other two subvortices are ready to fade away. The subvortices revolve around the overall vortex center rapidly, completing a full 360° evolution in about 1 min; we will use 3-s model output to track the movement of individual subvortex later. We note here that ζ in the subvortices in the southeastern part of the main vortex is generally larger through the period that they are clearly defined (Figs. 2g–o), and it is also true before the establishment of subvortices (Figs. 2b–d). This is related to the overall vortex asymmetry and would contribute to the wavenumber-1 wave energy, to be discussed next.

To investigate the amplitude and propagation of flow structures within the main vortex in terms of wave components, we perform Fourier decomposition of ζ in the azimuthal direction. Figure 3 shows the time series of wave energy of the wavenumber-0, -1, -2, -3, -4, and -5 components from 0711 through 0728 UTC. The wave energy is the square of wave amplitude.

From 0711:30 through 0717 UTC, wavenumber 1 dominates, except for several short moments between 0714 and 0715 UTC (Fig. 3) when it is overtaken by wavenumber 2. This asymmetry corresponds to the main vortex asymmetry seen in Fig. 2 during this period. Near 0718 and 0719 UTC, wavenumber 4 has the largest energy, because four subvortices are well established near these times (Figs. 2h,j). From 0719 until 0726:30 UTC, because of the establishment of the five strong subvortices, wavenumber 5 has the largest energy. This is the time period when the five subvortices are at their maximum intensities (Figs. 2k–n).

Between 0716 UTC, wavenumber 1 is the next strongest wave component, corresponding to the main vortex asymmetry seen in Fig. 2 during this period.

From 0711:30 until 0716 UTC except for some times near 0714 UTC, the energy of wavenumber 0 increases significantly (Fig. 3), corresponding to the organization and strengthening of the axisymmetric vortex ring (Figs. 2a–f). Its energy decreases somewhat as wavenumber-4 energy increases over the next 2 min. Apparently, the development of the four subvortices consumes some of the wavenumber-0 energy. After 0719 UTC, wavenumber-0 energy steadily increases again until after 0722 UTC when wavenumber-5 energy rapidly increases (Fig. 3). Likely, the strengthening of the axisymmetric mean circulation provides more favorable conditions for the five strong subvortices to develop, although most of time, the magnitude of wave energy of wavenumber 0 is smaller than that of wavenumbers 1, 4, and 5.

The strengths of wavenumbers 0 and 5 are generally maintained near their peak values that are similar between 0722 and 0724 UTC. After 0724, both wave components steadily decrease in energy (Fig. 3) and by 0728 UTC the tornado has essentially dissipated. Overall, there is a positive correlation between wavenumber-0 energy and wavenumber-4 or -5 energy, and the increase in wavenumber-0 energy generally precedes that of wavenumber 4 or 5. We will analyze the formation mechanism of the underlying wave components and corresponding subvortices in more detail in the next section to test the hypothesis that the subvortices develop primarily due to favorable wave instability conditions associated with the mean vortex, in particular the vorticity ring structure.

4. VRWs and their possible relation to the subvortices

a. Azimuthal propagation of VRWs

As indicated by Fig. 1a, when a vorticity ring structure is established within the tornado vortex, the sign of the radial gradient of vertical vorticity changes from positive to negative going outward across the ring (Fig. 4). This satisfies the necessary condition of barotropic instability. Rayleigh's generalized necessary condition requires that the radial gradient of vorticity changes

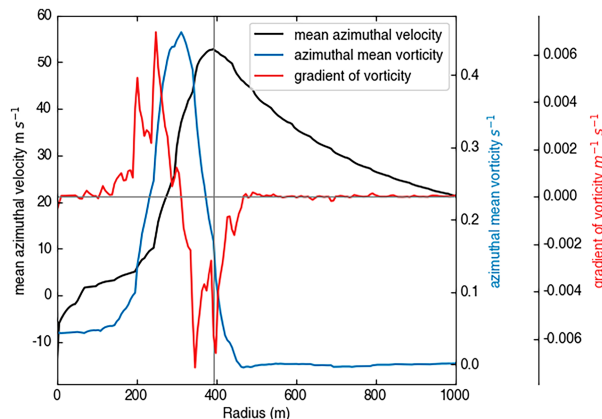


FIG. 4. The radius profile of azimuthal-mean tangential velocity (black; m s^{-1}), azimuthal-mean vorticity (blue; s^{-1}), and its gradient relative to radius (red; $\text{m}^{-1} \text{s}^{-1}$) at 0716 UTC and at ~ 26 m AGL. The horizontal gray line is the gradient of azimuthal mean vorticity equal to 0. The vertical gray line is the radius of maximum azimuthal-mean tangential velocity and is the position used to calculate VRWs' parameters.

sign, while Fjortoft's generalized necessary condition of instability requires negative correlations between the radial gradient of vorticity and azimuthal-mean tangential velocity on average (Montgomery and Shapiro 1995). The barotropic instability is exhibited as growing counterpropagating phase-locked VRWs along the vorticity ring. This inspires us to check if the characteristics of our simulated waves associated with subvortex development match those of unstable VRWs.

The dispersion relation of VRWs based on an idealized two-dimensional (2D) nondivergent barotropic vorticity equation for inviscid flow is, according to Montgomery and Kallenbach (1997),

$$\omega = n\bar{\Omega}_0 + \frac{n}{R} \frac{\bar{\zeta}'_0}{\left(k^2 + \frac{n^2}{R^2}\right)}, \quad (1)$$

$$k(t) = k_0 - nt\Omega'_0, \quad (2)$$

where ω , Ω , n , k , k_0 , R , and ζ are the frequency, angular velocity, azimuthal and radial wavenumbers, initial radial wavenumber, the radius of maximum azimuthal-mean tangential wind, and vorticity, respectively. The prime represents partial derivative with respect to radius r and overbar denotes azimuthal average. Subscript 0 denotes values at $r = R$. The sign of $\bar{\zeta}'$ is opposite on the two sides of the radius of maximum $\bar{\zeta}$ (Fig. 4); $\bar{\zeta}'$ is positive on the inner edge of the vortex ring so that the second term on the right-hand side of (1) is positive; thus, VRWs will propagate at a speed faster than the maximum mean tangential velocity (i.e., prograde relative to the mean flow) while VRWs on the outer edge with a negative $\bar{\zeta}'$ will propagate at a speed slower than the maximum mean tangential velocity (i.e., retrograde relative to the mean flow). The differential phase speeds allow the VRWs on the outer edge to be locked in phase with VRWs on the inner edge, even though the

tangential wind speed is larger at the outer edge. The interaction of the phase-locked VRWs provides the physical mechanism of barotropic instability on a shear zone (Schubert et al. 1999), which will be discussed further in section 4c.

Montgomery and Kallenbach (1997) further examined a 2D barotropic vorticity model with divergence, and obtained a dispersion relation that is in terms of the radial gradient of potential vorticity (PV). The relation was further generalized by McWilliams et al. (2003). Because for tornadoes, PV makes little sense; therefore, we will use Eq. (1) to calculate the parameters of VRWs for our simulation.

Previous studies have shown that the structure of tornado is dependent on the swirl ratio (S). Multiple vortices form for large S (Gall 1983; Davies-Jones 1986). The swirl ratio can be defined as $S = v_0/\bar{w}$, where v_0 is the tangential velocity at the edge of the updraft and \bar{w} is the mean vertical velocity through the updraft hole of the tornado simulator (Davies-Jones et al. 2001). Montgomery et al. (2002) suggested that for swirl ratio greater than unity, the two-dimensional model can provide qualitatively and quantitatively correct approximations to the growth rates and unstable modes, given that the flow is dominated by the tangential wind component. In our case, the swirl ratio is estimated to be greater than 3 (see details in section 6). Therefore, quasi-2D vortex dynamics can be applied to our problem. More discussion on this topic will be given later.

The radius of maximum mean tangential velocity is the radius that is often used to calculate parameters of VRWs, such as the frequency, group velocity, and phase speed, in hurricanes (Montgomery and Kallenbach 1997). This radius usually coincides with that of large negative radial gradient of vorticity (Wang 2002) in hurricanes, and is also true in our simulation (Fig. 4). We therefore also choose this radius to calculate the above parameters and the stagnation radius of VRWs. For these calculations, we will mainly focus on the time of 0716 UTC when the vorticity ring is best defined, and the waves/vortices are just about to develop. The vorticity in the simulated tornado is largest at the surface; therefore, we choose to mainly focus on the fields at the lowest model scalar level above ground (~ 26 m). Fields at 0724 UTC and at a higher level will also be examined to a less extent.

Although the discrete subvortices have not been established at 0716 UTC, the amplitude of wavenumber 5 is already relatively large and continues to increase with time (Fig. 5a). The radial wavelength for wavenumber 5 estimated subjectively based on the radius-time Hovmöller diagram is approximately 250 m (Fig. 5b), and k_0 is therefore about $2\pi/250 \text{ m}^{-1}$. The maximum mean tangential velocity is 52.8 m s^{-1} and its radius is 395 m at this time (Fig. 4). The azimuthal phase speed defined by $C_{p\lambda} = \omega R/n$ is 45.6 m s^{-1} . This result is not much different from that shown in Fig. 5a, where the subvortices take about 60 s to complete a circle, and its average tangential velocity is 41 m s^{-1} . This agrees with the characteristics of VRWs that the waves on the outer edge, which has a negative radial gradient of vorticity, will retrograde relative to the mean flow. The azimuthal phase speeds being slower

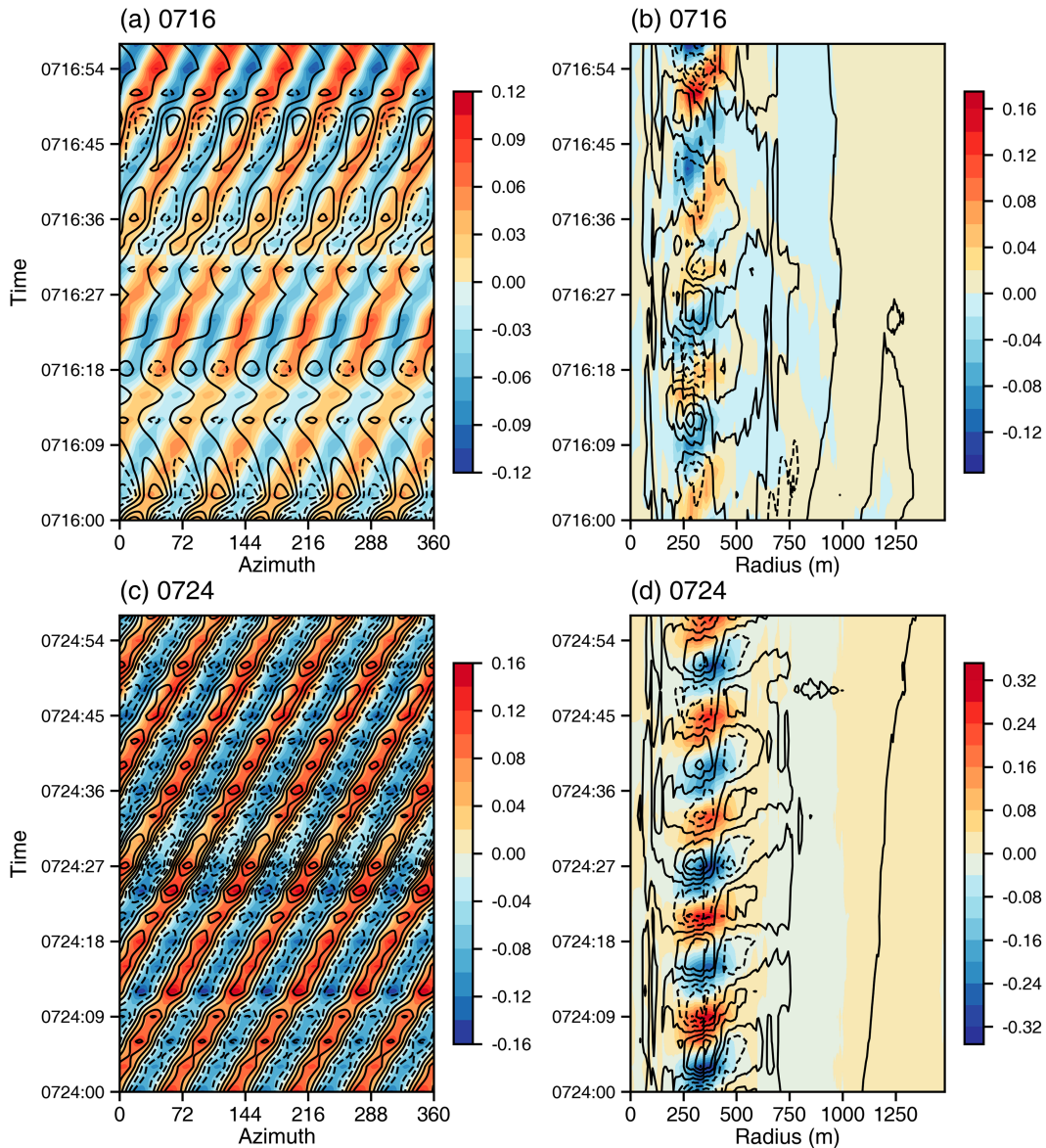


FIG. 5. (a) The time–azimuth (azimuth angles are 0° due east and 90° due north) Hovmöller diagram of wavenumber-5 ζ (shaded; s^{-1}) and w at 26 m AGL [black contours at (a) 0.08 and (c) 0.25 m s^{-1} intervals; positive solid and negative dashed] at the radius of maximum azimuthal-mean tangential velocity from 0716:00 to 0716:57 UTC. The horizontal axis is counterclockwise and shows a cyclonic rotation of the wavenumber-5 VRWs. (b) As in (a), but for time–radius Hovmöller diagram from the tornado center to a radius of 1500 m along the 270° azimuth angle (to the south), showing an outward propagation of the wavenumber-5 VRWs [the w contour intervals are (b) 0.3 and (d) 0.5 m s^{-1}]. Note that (c) and (d) are the same as (a) and (b), but for time period 0724:00–0724:57 UTC.

than the maximum wind speed also applies to wavenumbers 2–5. The same method can also estimate the wavelength of other wavenumbers. The estimated radial wavelengths for wavenumbers 1, 2, 3, and 4 are about 250, 229.2, 243.1, and 277.8 m (see Fig. A1 of appendix A), and the corresponding azimuthal phase speeds are 43.8, 45.5, 44.9, and 43.5 m s^{-1} , respectively. The corresponding azimuthal group velocities ($C_{g\lambda}$) for wavenumbers 1–5 calculated by Eq. (3) are 44.0, 46.0, 46.2, 46.6, and 48.6 m s^{-1} , respectively:

$$C_{g\lambda} = \frac{\partial \omega}{\partial (n/R)} = R\bar{\Omega}_0 + \frac{\bar{\xi}'_0}{\left(k^2 + \frac{n^2}{R^2}\right)^2} \left[k_0^2 - \frac{n^2}{R^2} (1 + r^2 R^2 \bar{\Omega}_0'^2) \right]. \quad (3)$$

The above results of azimuthal phase speeds are not consistent with the azimuthal propagation speed of the wave given by Lord Kelvin (Thomson 1880) on a Rankine vortex and summarized

by Lamb (1932) and Guinn and Schubert (1993). The formula of azimuthal phase speed is given as

$$c = V_{\max} \left(1 - \frac{1}{n} \right), \quad (4)$$

where V_{\max} denotes the maximum wind speed. Kuo et al. (1999) performed a two-dimensional nondivergence model simulation and found that the azimuthal phase speed calculated by Eq. (4) is consistent with the rotation speed of an elliptical eye in simulation. According to Eq. (4), the phase speed increases as wavenumber increases. While the azimuthal phase speeds of wavenumbers 1–5 calculated by Eq. (1) do not always increase with increasing wavenumber n . The azimuthal phase speed of wavenumber 4 is slower than those of wavenumbers 1, 2, and 3 in our simulation. This is because Eq. (1) is not only a function of azimuthal wavenumber n but also of radial wavenumber k . Note that the azimuthal phase speed of Kelvin wave is the same as Eq. (4) (Guinn and Schubert 1993), the feature that azimuthal phase speed slower than azimuthal-mean tangential velocity hence cannot discriminate between Kelvin waves on a Rankine vortex and VRWs. Previous studies have also found that the speed of subvortices in tornadoes is slower than the maximum mean tangential velocity, including radar observational studies (Bluestein et al. 2003; Tanamachi et al. 2007), idealized simulations (Ward 1972; Rotunno 1984; Lewellen et al. 1997), and a real case simulation (Mashiko and Niino 2017), but only Bluestein et al. (2003) suggest that this phenomenon is related to VRWs.

We also examined corresponding Hovmöller diagrams at ~ 322 m AGL (not shown). For the 0724 UTC time period, the propagation patterns are very similar to those of ~ 26 m, with w being larger and ζ being smaller at ~ 322 m. For the 0716 UTC time period, there are more differences between the two levels. At this time, the vortex is still dominated by wavenumber-0 and -1 structures and the wavenumber 5 is weak and less organized (Fig. 3). But still, the general behaviors of the wavenumber-5 waves, including their structures and propagation, are similar at the two levels and the two time periods, suggesting quasi-barotropic structures at the lower levels, and the waves at the later times are primarily the results of nonlinear amplification of earlier waves.

b. Radial propagation of VRWs

In real atmosphere like our case, the vorticity profile can be considered a smoothed version of the top-hat vortex ring (with a large constant vorticity within the ring that drops off to much smaller values on the two sides), and the profile of vorticity often not only satisfies the necessary condition of barotropic instability but also has vorticity gradient in the smoothly varying region outside the vortex ring (eyewall in hurricanes) that supports stable propagating VRWs. When the discrete waves on the two edges of the vortex ring are phased locked, barotropic instability can be activated, and the large amplitude VRWs due to nonlinear growth can provide perturbations to trigger sheared VRWs. Different from discrete VRWs that develop at the edges of the top-hat-type vorticity profiles that can become unstable, sheared VRWs are stable and can propagate radially

outward (Schechter and Montgomery 2007). Therefore, unstable phased-locked discrete VRWs at the vorticity ring and VRWs propagating in the more continuously sheared flows outside can coexist (Reasor et al. 2000) and they can be considered different types of VRWs. Although the radial propagation associated with sheared VRWs is not central to the formation of subvortices, we also calculate the parameters related to radial propagation, including radial phase speed C_{pr} , radial group velocities (C_{gr}), and the stagnation radius r_s , where radial group velocity goes to zero, to examine the outward-propagating characteristics of the waves that further help confirm their VRW nature. The formulas are given by Montgomery and Kallenbach (1997) as follows:

$$C_{\text{pr}} = \frac{\omega}{k}, \quad (5)$$

$$C_{\text{gr}} = \frac{\partial \omega}{\partial k} = \frac{-2kn\bar{\xi}'_0}{R\left(k^2 + \frac{n^2}{R^2}\right)}, \quad (6)$$

$$r_s = R + \frac{\bar{\xi}'_0}{R\bar{\Omega}'_0} \frac{1}{\left(k_0^2 + \frac{n^2}{R^2}\right)}. \quad (7)$$

For wavenumber 5, the radial phase speed is estimated to be about 23.0 m s^{-1} . The radial group velocity is about 5.9 m s^{-1} , respectively. As the wave packets propagate outwards, they are continually slowed down by the shearing flow, which would increase the radial wavenumber k , and thus the waves behave as spiral bands. Since the radial group velocity is proportional to $O(k^{-3})$ (Chen and Yau 2001), the radial propagation eventually ceases and the radius at which this happens is referred to as the stagnation radius (Montgomery and Kallenbach 1997). The calculated stagnation radius is 479.6 m for wavenumber 5, consistent with Fig. 5b. The wavenumber-5 components of ζ and w slant upward in the time–radius phase space, indicating outward phase propagation. Some of this is due to the shearing effect by the radially decreasing azimuthal flow, creating apparent phase propagation. The amplitudes of the waves decrease from the maximum at around 300 m radius and become very weak and hardly discernable beyond 500 m , indicating that wave energy ceases to propagate outward (at group velocity) at $\sim 500 \text{ m}$, the stagnation radius.

The above parameters also are calculated for the other four wavenumbers. Their radial phase speeds are 4.4 , 8.4 , 13.2 , and 19.5 m s^{-1} , their radial group velocities are 1.8 , 2.7 , 4.4 , and 7.1 m s^{-1} , and stagnation radii are 482.2 , 479.2 , 480.4 , and 483.7 m , respectively.

We show in addition the propagation characteristics of wavenumber 5 at 0724 UTC when the subvortices are in their most mature stage (Figs. 5c,d). The wavenumber-5 component of ζ is particularly large with a maximum value exceeding 0.16 s^{-1} . Compared with 0716 UTC, the outward wave propagation is more evident at 0724 UTC (Fig. 5d) when the subvortices are fully developed. Beyond 500 m , the wave amplitudes of ζ again become very small and the waves are

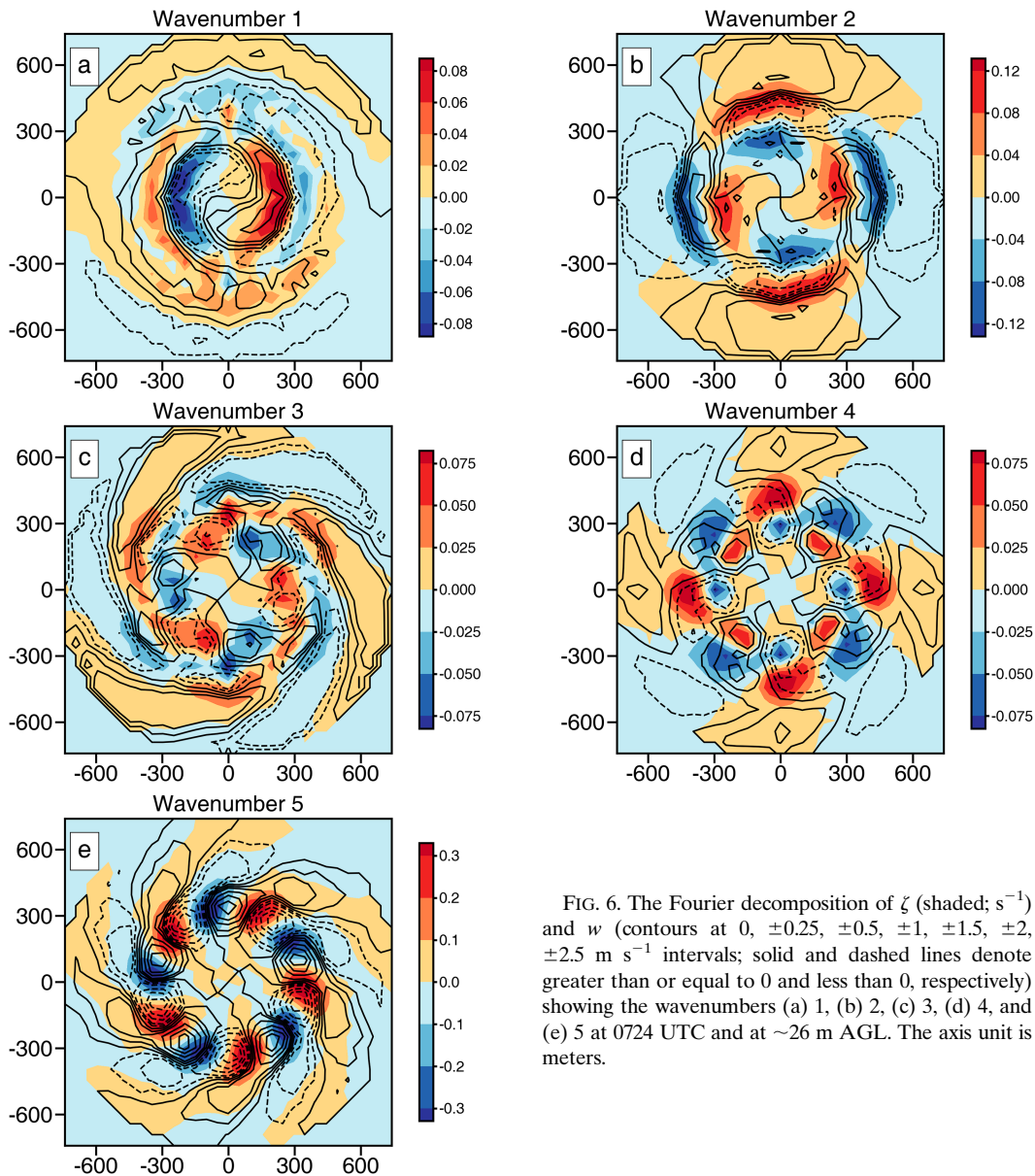


FIG. 6. The Fourier decomposition of ζ (shaded; s^{-1}) and w (contours at $0, \pm 0.25, \pm 0.5, \pm 1, \pm 1.5, \pm 2, \pm 2.5 \text{ m s}^{-1}$ intervals; solid and dashed lines denote greater than or equal to 0 and less than 0, respectively) showing the wavenumbers (a) 1, (b) 2, (c) 3, (d) 4, and (e) 5 at 0724 UTC and at $\sim 26 \text{ m AGL}$. The axis unit is meters.

hardly discernable. The parameters of VRWs, azimuthal and radial phase speed, azimuthal and radial group velocities, and stagnation radius, are also calculated for 0724 UTC (see appendix B). The azimuthal phase speed is consistent with the characteristics of VRWs, as at 0716 UTC. The values of radial phase speed of wavenumber 5 and stagnation radii of wavenumbers 1–5 are too large compared with reality. This may be because as the subvortices mature, nonlinear vorticity dynamics (stretching, etc.) start to play a significant role in affecting the tornado structure (more on this in section 7).

The estimation of radial wavelength has uncertainties (see appendix A) affecting the calculation of above parameters, especially for the radial and azimuthal group velocities. The radial group and azimuthal velocities are proportional to $O(k^{-3})$, and are more sensitive to the value of k . Still, the characteristics we

obtain are in generally good agreement with those of VRWs, substantiating the existence of VRWs.

c. Horizontal and vertical structures of wave components

Since the subvortices are just about to develop at 0716 UTC, we look at the decomposed fields at 0724 UTC when the five subvortices are most mature, to examine the wave structures. Although the linear theory at this time is not strictly applicable, the structures of VRWs remain mostly similar. We see that w leads ζ by about one-quarter of a full phase for wavenumbers 1–5 in both azimuthal and radial directions (Fig. 6). It is the most evident for wavenumber 5 (Fig. 6e) while for other wavenumbers it is less consistent (Figs. 6a–d). While near the radius of maximum mean tangential wind, w and ζ are in phase, as seen in Figs. 5a and 5c. The possible reason is that the structure

of subvortices at this time are significantly affected by nonlinear vorticity dynamics including tilting and stretching processes (see details in section 7). The characteristic that the phase of w leads that of ζ by about one-quarter of a full phase is similar to that of midlatitude Rossby waves. Wang (2002) also noted this structure in his tropical cyclone simulations. Another pronounced feature with the vertical velocity fields is the cyclonically inward spiraling bands of w . This feature is most clear with wavenumbers 3–5 (Figs. 5b,d and 6c–e), similar to the structure of sheared VRWs in Fig. 6 of Montgomery and Kallenbach (1997). The positive bands are what support the spiral rainbands in tropical cyclones (Hall et al. 2013), and they are also enhanced by precipitation along the rainbands (Wang 2002). Without similar enhancement, the w bands in tornadoes tend to be weak, but their significance in affecting the low-level flow structure of tornado vortices is worth exploring in the future.

To see the sensitivity of the wave pattern and propagation to the height level, we further show the Fourier decomposed ζ and w at ~ 322 m, near the top of the strong vorticity ring, in Fig. C1 of appendix C, which correspond to the fields at ~ 26 m in Fig. 6. The patterns of the decomposed ζ and w are similar between the two levels (cf. Figs. 6 and C1), especially for wavenumbers 2 and 5. For wavenumbers 1, 3, and 4, the spiral structure of w can be seen as well and is more prominent at ~ 322 m (mainly because w is larger at ~ 322 m). The characteristic that the phase of w leads that of ζ by about a quarter phase in both radial and azimuthal directions exists at both levels, especially for wavenumber 5. The similar structures between the two levels confirm the quasi-barotropic nature of the wave disturbances. Besides, there is a slight phase lag at the ~ 322 m compared to the ~ 26 m, suggesting upward propagation of disturbances from the lower levels. These results suggest that the disturbances at these two levels are closely coupled, and they originate from the same physical mechanism.

The above results only focus on horizontal planes; we draw height–azimuth diagrams of wavenumber 5 of ζ and w along the radius of maximum azimuthal-mean tangential wind of different levels at 0716 UTC to see how the wave disturbances propagate in the vertical (Fig. 7, top). Below ~ 400 m, the wave structures are nearly upright (Fig. 7a), suggesting again that the structures can be regarded as quasi barotropic. Different from 0716 UTC, there is more vertical tilt with wavenumber 5 below 400 m at 0724 UTC (Fig. 7, bottom panels). This tilt may be because of nonlinear interaction of the fully developed subvortices and the azimuthal mean flow, and differential advection of the subvortices by the vertically decreasing tangential flow. Still, the general structures of the wavenumber-5 mode are similar at the two levels, except for a slight phase lag at the higher level.

Above 400 m, the waves are clearly tilted rearward relative to the tangential flow, implying upward propagation of the wave disturbances. Besides, the azimuthal phase of w leads that of potential temperature θ by about one-quarter of a full phase at 0716 UTC, which is most evident between 2000 and 2500 m (Fig. 7b). This is characteristic of internal gravity waves (IGWs). The stratification is stable at those levels, supporting IGWs. Previous studies also found that VRWs in hurricanes can excite internal IGWs when the

Rossby number is greater than unity and IGW emissions can promote VRWs to grow (Schechter and Montgomery 2007). The one-quarter phase difference between w and θ , however, cannot be seen at 0724 UTC (Fig. 7d); this may be because as the vertical motion becomes stronger at 0724 UTC, the direct effects of upward and downward advection of θ start to play more dominant roles (creating negative θ where w is positive). The relationship between VRWs and IGWs needs exploration in future work.

Compared to VRWs that develop within tropical cyclones, those within tornado vortices can develop into much larger amplitude and form well-defined, intense discrete subvortices. Within tropical cycles, VRWs mainly exhibit themselves in the form of polygonal eyewalls (Reasor et al. 2000; Chen and Yau 2001; Kossin et al. 2002; Li and Wang 2012; Li et al. 2019), presumably because the core vortex in tropical cyclones is less unstable and/or the mean azimuthal circulation is more dominant. A detailed comparison of the two is outside the scope of this study.

5. VRW instability as a cause of the nonlinear development of subvortices

Schubert et al. (1999) performed a linear stability analysis for an idealized vorticity ring with a top-hat vorticity radial profile. They used two parameters, termed thickness and hollowness later by Hendricks et al. (2009), to quantitatively describe the shape of the vorticity ring and explore their effects on the vorticity redistribution by barotropic instability. The thickness is defined as the ratio of the inner (r_1) and outer (r_2) radii of the ring, or $\delta = r_1/r_2$. The hollowness is defined as the ratio of the vorticity in the inner region to that of the area-weighted average of vorticity out to edge of the vorticity ring, denoted as $\gamma = \zeta_{\text{inner}}/\zeta_{\text{av}}$. δ and γ measure the width of the vorticity ring and the relative magnitude of ζ on the vortex ring, respectively. The vorticity outside the ring is set to zero in their model. Schubert et al. (1999) rewrote the frequency equation of VRWs that only includes n , δ , and γ as follows:

Dimensionless complex frequency

$$= \frac{1}{4} \left(n + (n - 1)\gamma \pm \left\{ \left[n - (n - 1)\gamma - 2 \left(\frac{1 - \gamma\delta^2}{1 - \delta^2} \right) \right]^2 + 4 \left(\frac{1 - \gamma\delta^2}{1 - \delta^2} \right) \left(\gamma - \frac{1 - \gamma\delta^2}{1 - \delta^2} \right) \delta^{2n} \right\}^{1/2} \right). \tag{8}$$

Equation (8) mathematically depicts the interaction of two counterpropagating discrete waves, the frequencies of which can be estimated using Eq. (1). When the frequency of the combined waves given by (8) contains a nonzero positive complex part, the waves are unstable. The imaginary part of Eq. (8) is a dimensionless measure of the growth rate of waves. Clearly, the end state of the vorticity field is sensitive to δ and γ . When the vorticity ring is thinner (i.e., for a larger δ) and more filled (i.e., for a larger γ), the growth rate of unstable waves is larger and the most unstable azimuthal wavenumber is higher. Based on

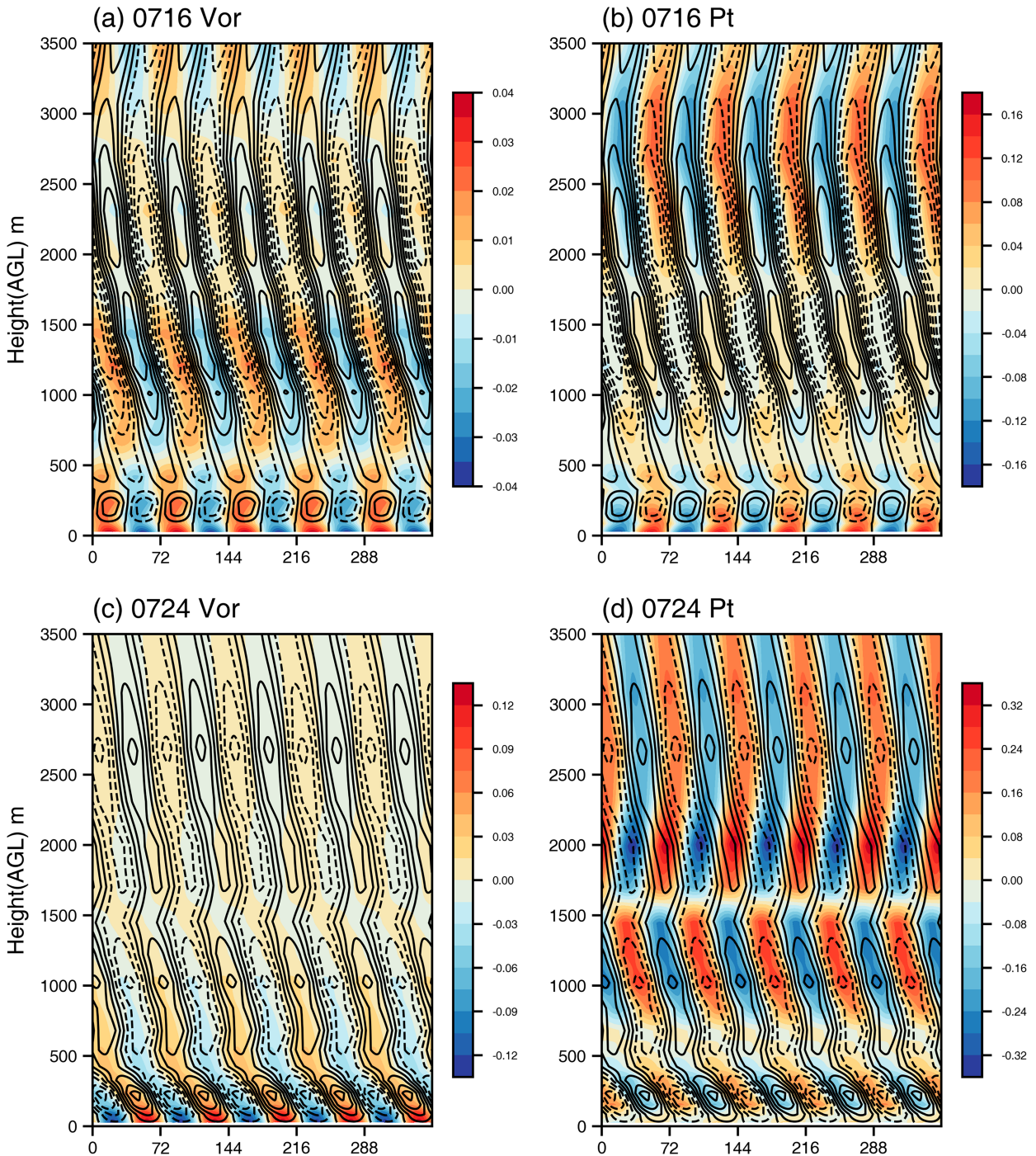


FIG. 7. Wavenumber-5 disturbances of (a) vertical vorticity ζ (shaded; s^{-1}) and (b) potential temperature θ (shaded; K) in an azimuthal-vertical plane along the radii of maximum azimuthal-mean tangential wind of different levels, at 0716 UTC, together with vertical velocity w (black contours at 0.4 m s^{-1} intervals; positive solid and negative dashed). (c),(d) As in (a) and (b), but at 0724 UTC (black contours at 1 m s^{-1} intervals).

Eq. (8), they examined 170 different vorticity rings sampling 10 different values of hollowness and 17 values of thickness, and obtained isolines of maximum growth rate and related most unstable wavenumber for different δ and γ (see Fig. 2 in

Schubert et al. 1999). Hendricks et al. (2009) obtained results similar to those of Schubert et al. (1999) using a pseudospectral model, but with some differences (Fig. 8). The estimation of the most unstable wavenumber is based on

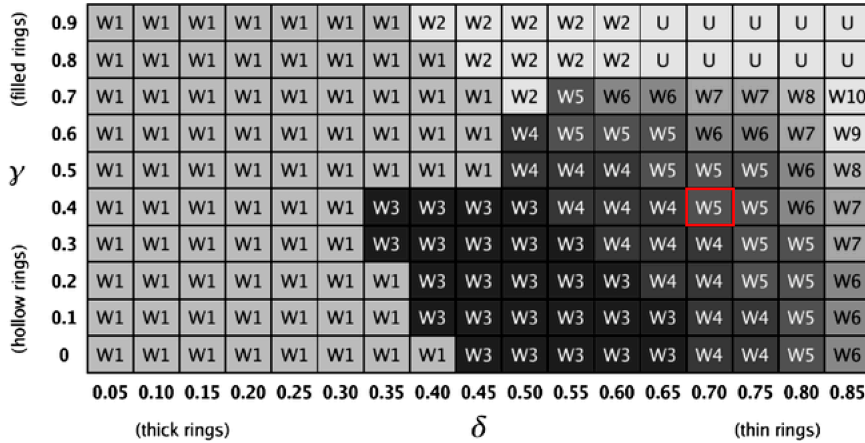


FIG. 8. Fastest-growing wavenumber instability at different δ (abscissa) and γ (ordinate). The U signifies that the initial wavenumber of the instability is not easily determined by visual inspection. Figure reproduced from Hendricks et al. (2009). The corresponding fastest-growing wavenumber in our simulation is denoted with a red rectangular box.

the assumed solutions for VRW eigenvalues in Schubert et al. (1999), while the results in Hendricks et al. (2009) are derived through simulation. The differences between Schubert et al. (1999) and Hendricks et al. (2009) may be attributed to the fact that the vorticity in the outside region ($r \geq r_2$) is not zero while positive in the results, as shown in Hendricks et al. (2009) (Tervey and Montgomery 2002). The unstable modes of wavenumbers 1 and 2 do not exist in the former but are present in the latter. For a given ring thickness, the pseudospectral model tends to generate slightly higher wavenumbers than those produced by linear stability analysis. Hendricks et al. (2009) also derived the end states (at $t = 48$ h for hurricane applications) given by different δ and γ and found that for very thin and relatively hollow rings, multiple subvortices can persist for over 15 h for hurricane-scale vortices. The work of Hendricks et al. (2009) represents a more complete summary of the non-linear vorticity dynamics for a range of parameter values than Schubert et al. (1999). We therefore choose to base our analysis on the results of Hendricks et al. (2009).

Both of the above studies are based on idealized 2D simulations, and their vorticity fields are axisymmetric at the beginning. Our simulated tornado has the most symmetric vorticity ring at 0716 UTC and has the largest radial gradient of tangential wind, and barotropic instability is likely the strongest at ~ 26 m where ζ is largest; we therefore choose this time and level to estimate the most unstable wavenumber given the vortex structure. The vorticity field at 0716 UTC is reproduced in Fig. 9a, together with two red circles defining the inner and outer edges of the vorticity ring. The vorticity field

at 0724 UTC, when the 5 subvortices are fully developed, is reproduced in Fig. 9b. Substituting the calculated thickness, 0.73, and hollowness, 0.47, at 0716 UTC into Eq. (8), the most unstable wavenumber is found to be 5 and its growth rate is 0.14. The most unstable wavenumber matches the graphic results produced by Hendricks et al. (2009) (Fig. 8), which show the largest growth rates for different δ and γ , agreeing with the result of our simulation a few minutes later (Fig. 8b). The results also further confirm that the formation mechanism of multiple subvortices within tornadoes is barotropic instability as in hurricanes (Schubert et al. 1999). Tervey and Montgomery once used the data by Lee and Wurman (2005) to perform a linear barotropic stability analysis on the Mulhall tornado profile and found wavenumber-2 and -3 instabilities (conference presentation, M. Montgomery 2023, personal communication). We note here that the inner or outer radii we chose to calculate δ and γ may introduce some uncertainties in determining the most unstable wavenumber. In the next section, we will perform an analysis of perturbation kinetic energy sources to further substantiate the barotropic instability mechanism.

6. Energetics of unstable waves

Following Walko and Gall (1984), Nolan (2005), and Nolan (2012), we calculate the rate of change of total perturbation kinetic energy E' for three-dimensional asymmetric perturbations to a symmetric vortex:

$$\frac{\partial E'}{\partial t} = \int \int \left\{ \left[\bar{v} \frac{1}{r^2} \frac{\partial}{\partial r} (\overline{r^2 u' v'}) \right]_{vr} + \left[\bar{w} \frac{1}{r} \frac{\partial}{\partial r} (\overline{r u' w'}) \right]_{wr} + \left\{ \bar{u} \left[\frac{\partial}{\partial r} (\overline{u' u'}) + \frac{\overline{v' v'}}{r} \right] \right\}_{ur} + \left[\bar{v} \frac{\partial}{\partial z} (\overline{v' w'}) \right]_{vz} + \left[\bar{w} \frac{\partial}{\partial z} (\overline{w' w'}) \right]_{wz} + \left[\bar{u} \frac{\partial}{\partial z} (\overline{u' w'}) \right]_{uz} + \left[\overline{u' F'_r} + \overline{v' F'_\lambda} + \overline{w' F'_z} \right]_F \right\} 2\pi r dr dz, \tag{9}$$

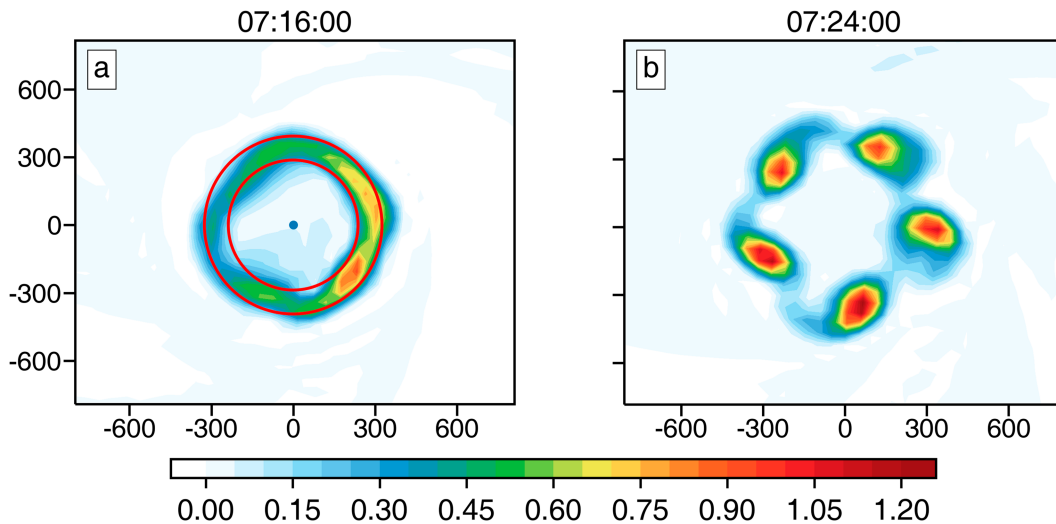


FIG. 9. (a) The initial state of ζ (s^{-1}) to calculate the hollowness and thickness at 0716 UTC and (b) the corresponding splitting structure at 0724 UTC. The inner and outer red circles in (a) are the inner and outer radii of the vorticity ring, respectively. The axis unit is meters.

where u , v , and w are radial, azimuthal (tangential), and vertical components of wind. The overbar denotes azimuthal average as in section 4. Different from section 4, the primes here represent perturbations with respect to azimuthal average. The F_r , F_λ , and F_z terms are frictional tendencies of the wind components. The terms in the equation are grouped into brackets, labeled, and represent different eddy fluxes transporting momentum between the mean and perturbation flows. Positive terms mean growth in perturbation kinetic energy, which can happen, for example, when momentum is transported from a faster mean flow to a slower mean flow.

In the radius–height plane, the patterns of total E' tendency [left side of Eq. (9), Fig. 10h] and the terms associated with radial shear of azimuthal wind (vr) (Fig. 10b) are quite similar, implying that vr is the primary production term of E' (Fig. 10b). The second largest contribution term is related to vertical shear of azimuthal wind (vz) (Fig. 10f). There are positive contributions near the center of vorticity ring (black contours in Fig. 10); however, the positive contributions are offset by negative vr term near the outer edge of vortex ring. Other terms, those associated with the radial shear of radial and vertical wind (ur and wr ; Figs. 10a,c) and vertical shear of radial and vertical wind (uz and wz ; Figs. 10e,g), are much smaller than vr and vz (Figs. 10b,f). The reason is that the magnitude of azimuthal-mean azimuthal winds are greater than 30 and even reach 45 m s^{-1} at the low levels (green lines in Fig. 10). Although the values of radial wind (blue lines in Fig. 10) can reach -16 m s^{-1} outside the outer edge of the vorticity ring and the values of w (red lines in Fig. 10) can reach 18 m s^{-1} in upper levels, the values of azimuthal-mean radial and vertical wind are, respectively,

only about ± 2 and $\sim 13 \text{ m s}^{-1}$ at the low levels near the center of vorticity ring. Therefore, at the location of the vorticity ring, the azimuthal winds still dominate, and the vertical velocity and radial inflow are also weaker close to the ground. The friction terms acting to reduce E' are small (Fig. 10d). The fact that the radial shear of azimuthal wind contributes the most to perturbation kinetic energy is consistent with the nature of barotropic instability (Staley and Gall 1979). This further substantiates that barotropic instability theories based on two-dimensional models of idealized vortices capture the essence of physical mechanisms, and the nonlinear growth of VRWs due to barotropic instability is the primary cause of the subvortex formation in multivortex tornadoes.

7. The main source of subvortex vorticity

Within nondivergent 2D models, barotropic instability only redistributes vorticity but does not create net vorticity. Within tropical cyclones, the production of potential vorticity, the amplification of VRWs, and the development and maintenance of spiral rainbands are substantially aided by latent heat release within the eyewall and rainbands (e.g., Chen and Yau 2001). In tornado cases, even though latent heating associated with positive spiraling w bands is generally absent, nonlinear vorticity dynamics can play a significant role in the amplification of VRWs given that vertical acceleration and therefore stretching can be large near the ground. We would like to know the main production source of vorticity for the intensification and maintenance of the subvortices.

The equation of vertical vorticity ζ is

$$\frac{\partial \zeta}{\partial t} = -\nabla \cdot v_h \zeta - \frac{\partial w \zeta}{\partial z} + \omega_h \cdot \nabla_h w + \zeta \frac{\partial w}{\partial z} + \frac{1}{\rho^2} \left(\frac{\partial \rho \partial p}{\partial x \partial y} - \frac{\partial \rho \partial p}{\partial y \partial x} \right) + \left(\frac{\partial F_y}{\partial x} - \frac{\partial F_x}{\partial y} \right). \quad (10)$$

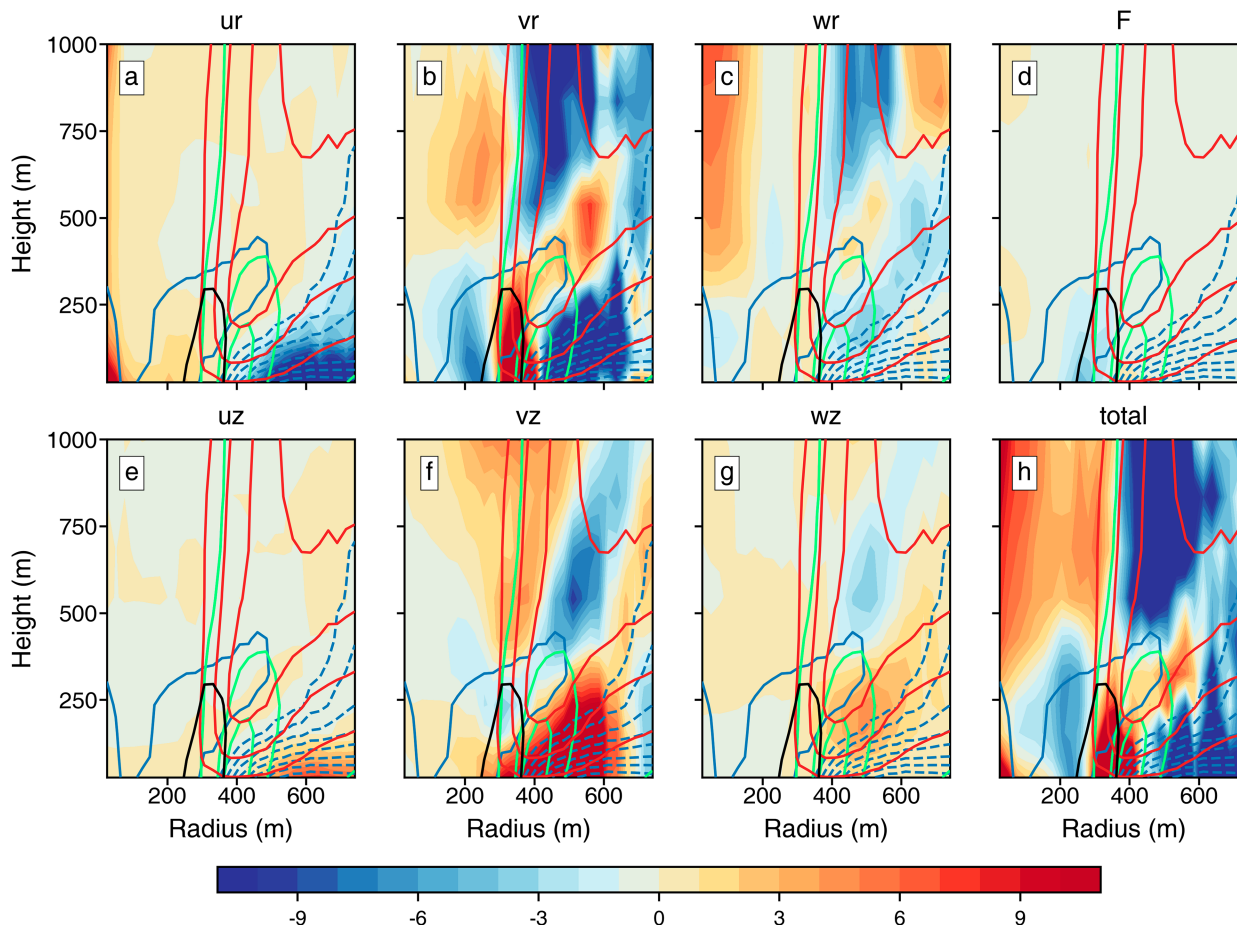


FIG. 10. Perturbation energy production by (a) ur term, (b) vr term, (c) wr term, (d) F term, (e) uz term, (f) vz term, (g) wz term, and (h) total energy production of the above terms at 0716:00 UTC (color shading). Black contour in each subplot is azimuthal-mean vertical vorticity denoting position of vorticity ring (contours at 0.3 s^{-1}). Also shown are the azimuthal-mean tangential wind (green contours at 30, 45, and 50 m s^{-1}), radial (blue contours at 2 m s^{-1} intervals; solid for positive and dashed for negative; the minimum contour is -16 m s^{-1}), and vertical velocity (red contours at 3, 8, 13, and 18 m s^{-1}).

The terms on the rhs of (10) are, in order, horizontal advection term in a flux form, vertical advection in a flux form, tilting of horizontal vorticity, stretching of vertical vorticity, baroclinic generation due to horizontal buoyancy gradient, and frictional generation due to horizontal gradient of frictional stress. We neglect the Coriolis force at the tornado scale.

The vorticity ring breaks up and evolves into five subvortices from 0716 to 0720 UTC (Figs. 2f–j). The vertical vorticity significantly strengthens during this stage. The subvortices are in their mature stage, reaching and maintaining their maximum intensity from 0720 to 0724 UTC (Figs. 2j–n). We select 0718 and 0721 UTC from the two stages to calculate the terms in (10) at the $\sim 26 \text{ m}$ level or the first scalar model level above ground (Figs. 11 and 12). The largest are clearly the horizontal advection (Figs. 11b and 12b) and vertical stretching terms (Figs. 11d and 12d) at both times. Horizontal advection is at least an order of magnitude larger than other terms; therefore, the sum of all terms (Figs. 11a and 12a) is very similar to the horizontal advection (Figs. 11b and 12b) in pattern. This is because of the rapid revolution of the subvortices around the

main vortex center, causing large local tendencies in vorticity. However, horizontal advection only moves vorticity from one location to another and does not create or destroy vorticity by itself and is therefore not a true source/sink. The vertical vorticity stretching is therefore the largest source/sink (or more accurately the amplification) term that is mostly positive, especially at the outer edge of the subvortices when w is positive and large (Figs. 11d and 12d). The stretching term is responsible for the initial strengthening, and later maintenance of the subvortices from 0720 to 0726 UTC (not shown). The tilting term (Figs. 11e and 12e) is mostly positive, especially in the outer edge of the vorticity ring or near the subvortex centers. The tilting term is actually the true source of vertical vorticity, converting horizontal vorticity into vertical, and the horizontal vorticity near ground is often large due to surface drag (Roberts et al. 2016).

The vertical advection of ζ is the largest vorticity sink term, having the same magnitude as stretching. The term is generally negative where w is positive and vice versa (Figs. 11c and 12c) so its pattern is opposite to the stretching term, and

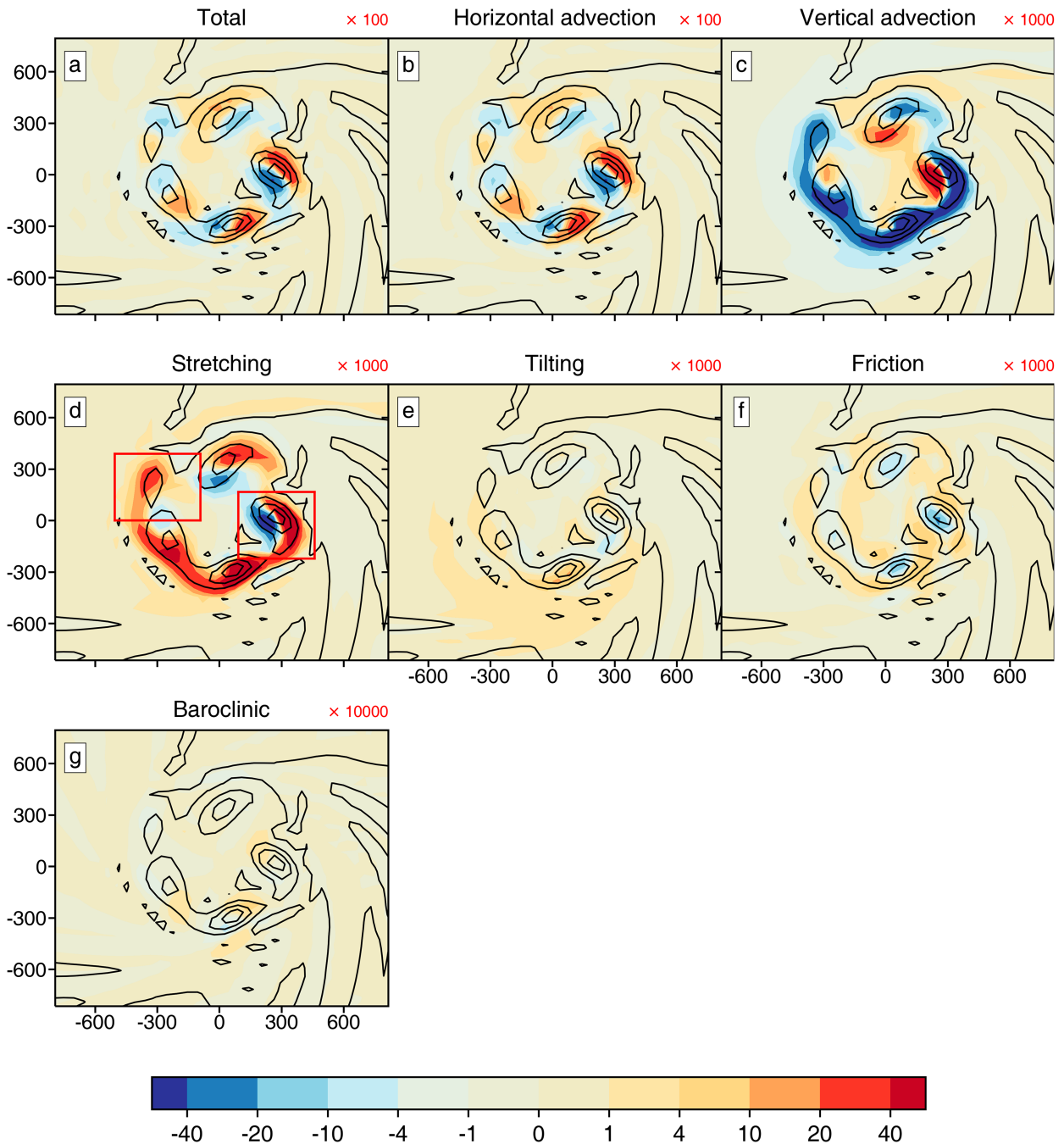


FIG. 11. ζ (contours at 0, 0.3, 0.6, 0.9, 1.2, 1.5 s^{-1}) and its production terms (shaded; s^{-2}) at 0718 UTC and ~ 26 m AGL, including (a) the sum of contribution terms, (b) horizontal advection, (c) vertical advection, (d) stretching, (e) tilting, (f) baroclinic, and (g) friction terms. Red boxes in (d) indicate the region for zooming in in Fig. 13. The corresponding multiplication magnitude of each term for better displaying the results is displayed on the right side of the title. The axis unit is meters.

this is particularly true for this first level above ground. This is because at the lower boundary of this layer, i.e., at the ground level the vertical advective flux of ζ is zero while the flux at the upper boundary of this layer is directed upward when w is positive, taking away vorticity from this layer. Thus, vertical advection acts to remove vorticity from the lower levels,

which is produced there by tilting then stretching in the outer edge of subvortices. Friction is the second largest vorticity sink, especially inside the subvortices (Figs. 11f and 12f). The baroclinic term is at least an order of magnitude smaller than other terms (Figs. 11g and 12g) and its contribution can be ignored. In summary, the tilting term is the true source of new

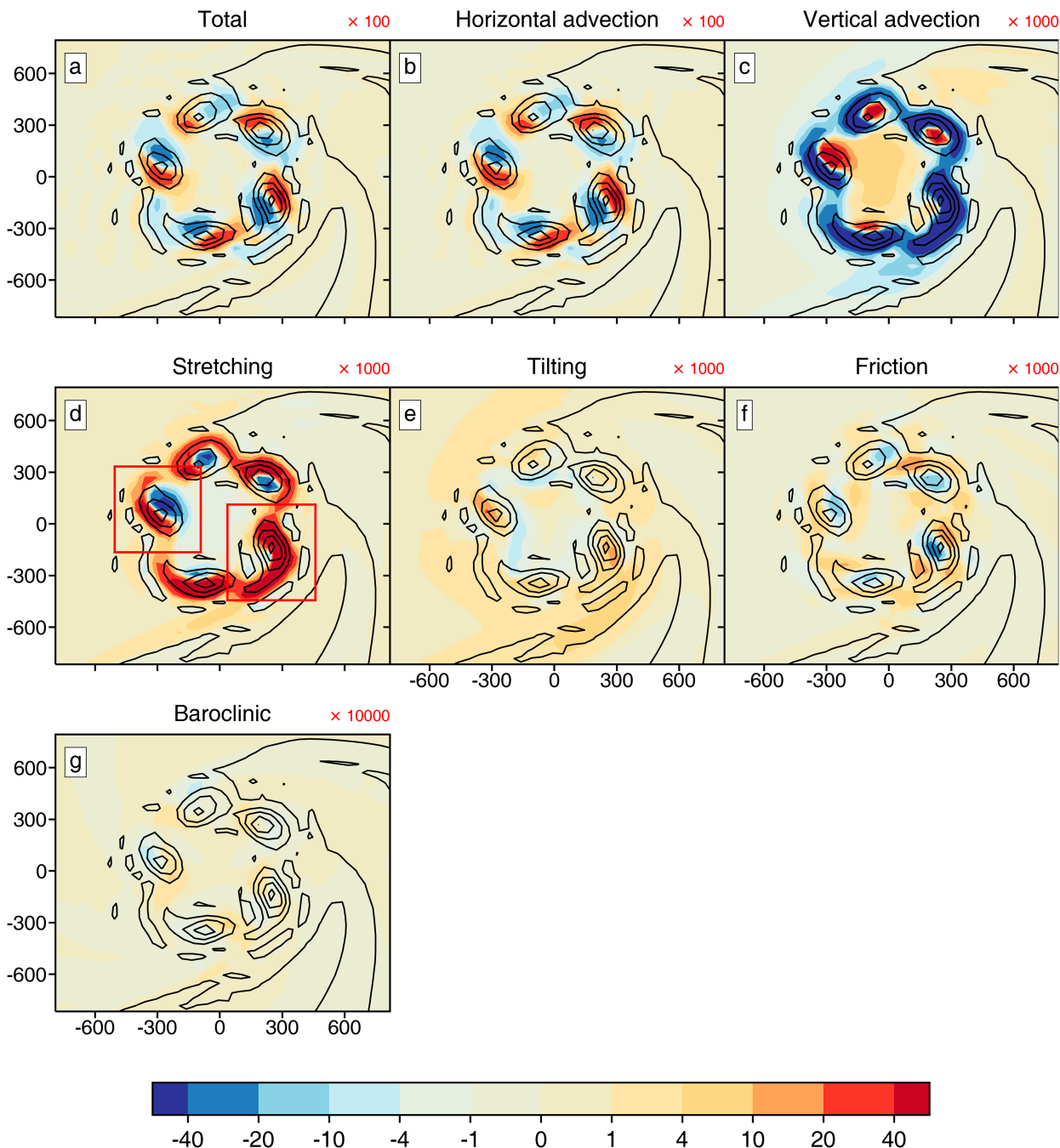


FIG. 12. As in Fig. 11, but for 0721 UTC.

vertical vorticity while the stretching term is the most important term to intensify and maintain the subvortices by offsetting reduction by friction and vertical advection.

We also note that the distribution of ζ is asymmetric among five subvortices, whose intensity can differ too. The subvortices in the southeast quadrant are stronger than those in the northwest quadrant of the main vortex (Figs. 11 and 12). As the subvortices revolve around, they strengthen as they enter the southeast quadrant and weaken as they move to the northwest

quadrant (evolution not shown). This phenomenon persists from 0716 to 0726 UTC (Figs. 2f–o). From Figs. 11 and 12, we can see that the stretching term is larger in the southeast than in the northwest quadrant, which is the main reason for the asymmetric and periodic distribution of ζ . Other terms do not have such prominent asymmetries and have less impact on ζ . To see it more clearly, we further zoom in onto the subvortices located in the southeast and northwest quadrants (Fig. 13). The stretching term in the southeast quadrants exceeds 0.06 and even reaches

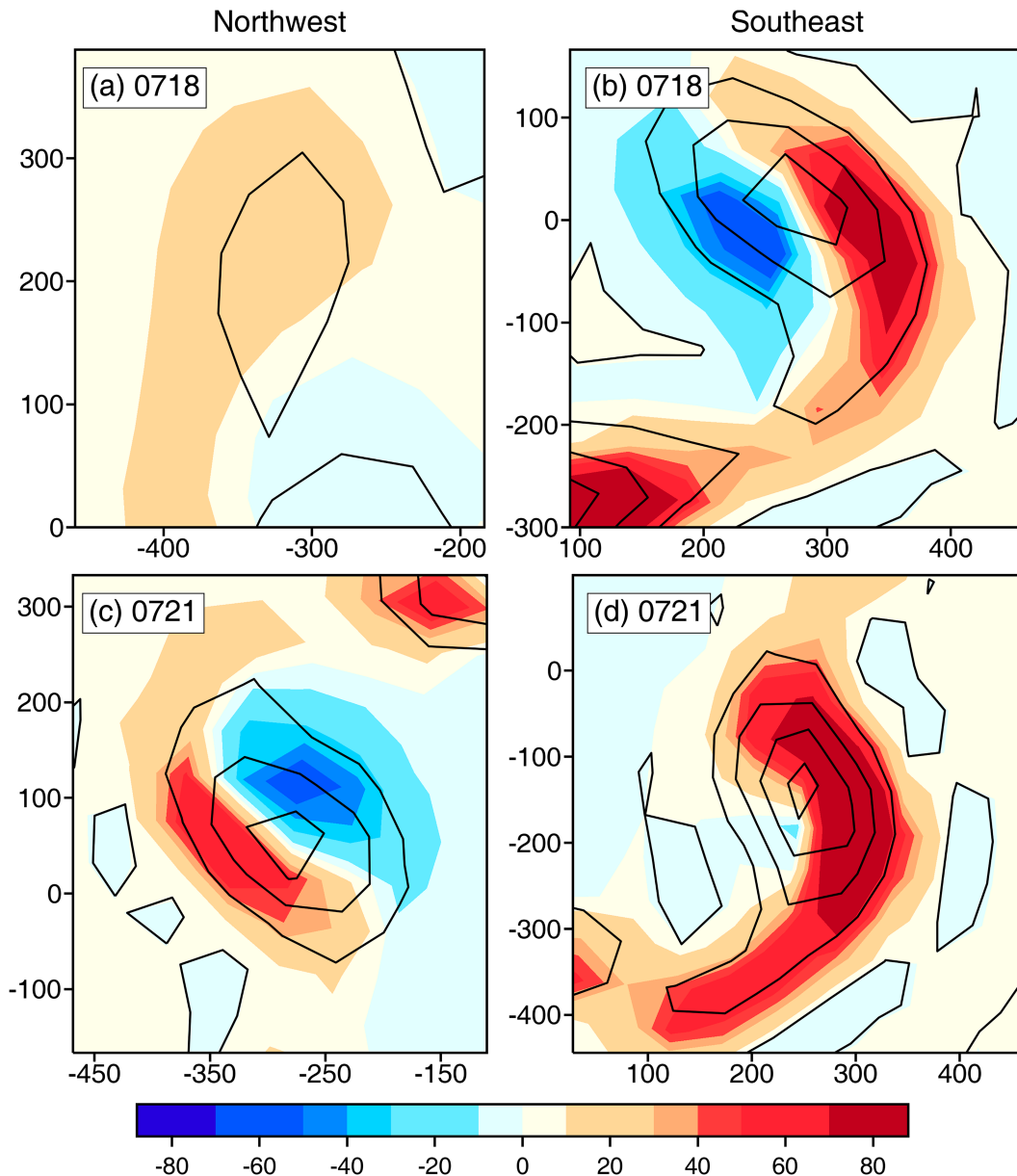


FIG. 13. As in Fig. 11, but showing only stretching terms (shaded; s^{-2}) and ζ (contours at 0, 0.3, 0.6, 0.9, 1.2, 1.5 s^{-1}) at (a),(b) 0718 and (c),(d) 0721 UTC. Panels are zoomed in the (left) northwest and (right) southeast relative to Figs. 11 and 12. The stretching term is multiplied by 1000 as in Figs. 11 and 12.

0.08 s^{-2} (Figs. 13b,d) while that in the northwest quadrant is much smaller with the maximum being less than 0.06 s^{-2} (Figs. 13a,c). The area of positive stretching term in the southeast is also larger at both times. This pattern of increasing eddy intensity as they traverse a region of enhanced vertical velocity was recognized earlier for eyewalls, inner-core disturbances, and primary rainbands in hurricanes, with wavenumber-1 VRW, attributed as the cause (Braun et al. 2006; Li and Wang 2012; Hall et al. 2013). We believe the same process is at work in our case.

To confirm, the total w and its wavenumber-1 component are shown in Fig. 14. Between 0716 and 0718 UTC (Figs. 14a,b), the

positive wavenumber-1 component of w almost coincides with positive w . Near and outside the radius of subvortex centers (the red circles in Fig. 14), the southern part of wavenumber 1 is larger than the northern part. After 0718 UTC, the wavenumber-1 component of w and total w in the south-southeast are still larger than those in the north-northwest (Figs. 14c-f). Consequently, w is intensified as air parcels rotate into the southeast side but is suppressed on the northwest side of the vortex, leading to larger vertical vorticity stretching on the southeast side than on the northwest side and hence the same asymmetric pattern of ζ as w (Fig. 13). Furthermore, the larger w right outside the radius of

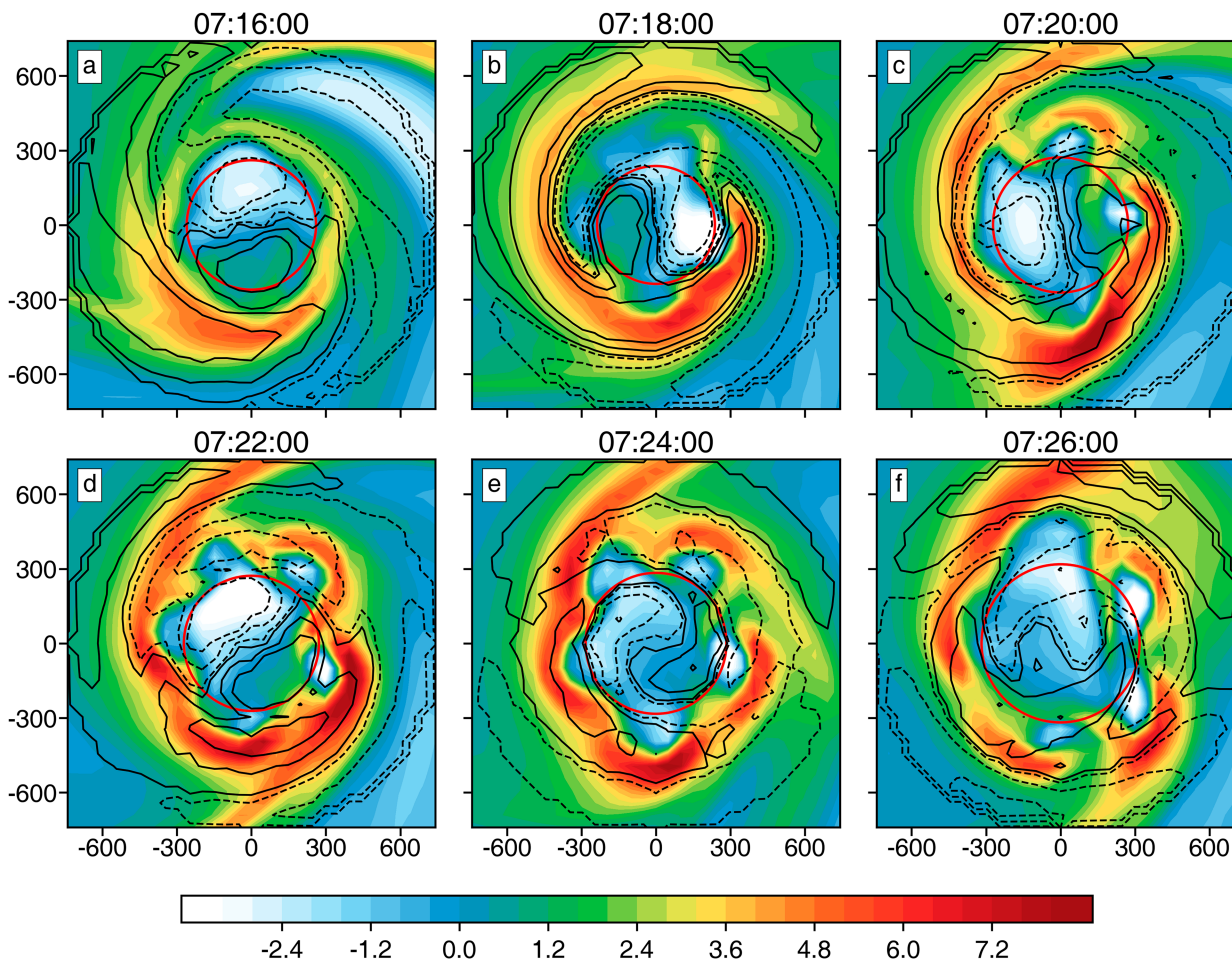


FIG. 14. w (shaded, m s^{-1}) and its azimuthal wavenumber-1 component (contours at ± 0.1 , ± 0.6 , $\pm 1.2 \text{ m s}^{-1}$ intervals; solid and dashed lines denote positive and negative, respectively) at $\sim 26 \text{ m}$ AGL from 0716 to 0726 UTC every 2 min. Red circles denote the radial position of the subvortex centers. The axis unit is meters.

subvortex centers will also create larger horizontal vorticity tilting. Therefore, azimuthal wavenumber 1 appears to play a similar role in modulating subvortex intensities in tornadoes, as it does in modulating the structure of near-core spiral rainbands and eyewalls in tropical cyclones.

8. Summary

A rare EF4-intensity occurred in Funing County, Jiangsu Province, China, on 23 June 2016, and the damage survey suggested there were subvortices (also called suction vortices) within the tornado (Meng et al. 2018). Sun et al. (2019) documented a rather successful simulation of this case using multiple levels of nested grids of the WRF-ARW Model, with the innermost grid of 48 m grid spacing simulating the life cycle of the tornado reaching EF3 intensity, and five subvortices developed in the mature stage of simulated tornado and lasted for more than 10 min. In this study, we rerun the simulation of Sun et al. (2019) and output data every 3 s to perform detailed analyses of the formation and maintenance mechanisms of the subvortices.

Before developing the subvortices, the tornado first establishes a one-cell structure with a vorticity maximum located at the tornado vortex center. It then evolves into a two-cell structure where the vorticity maximum is shifted away from the vortex circulation center to be located within a vorticity ring. The radial profile of vorticity ring satisfies both Rayleigh's and Fjortoft's generalized necessary conditions of barotropic instability. Barotropic instability results from the interaction of counterpropagating phase-locked discrete VRWs. The simulated subvortices retrograde relative to the maximum azimuthal-mean tangential velocity. The estimated azimuthal propagation speeds of wavenumbers 1–5 of subvortices are close to that given by the azimuthal phase speed of VRWs from Montgomery and Kallenbach (1997). Previous studies on hurricanes also found polygonal eyewall or mesovortices propagate at speeds less than the maximum azimuthal-mean tangential velocities (Thomson 1880; Lamb 1932; Walko and Gall 1984; Schubert et al. 1999; Kossin and Schubert 2001; Reasor and Montgomery 2001), conforming to the characteristics of VRWs. In addition, the phase of vertical velocity leads that of vertical vorticity by

about one-quarter of a full phase for Fourier-decomposed wavenumbers 1–5 in both azimuthal and radial directions. The unstable discrete waves can provide perturbations that trigger propagating VRWs in the more continuously sheared flow outside with a negative radial vorticity gradient. The characteristics of vertical velocities of the waves spiraling cyclonically inward are similar to those of the outward-propagating spiral rainbands supported by VRWs in hurricanes (Chen and Yau 2001). The waves with noticeable amplitude are confined within a radius of about 480 m, close to the theoretically estimated stagnation radius where the radial group velocity goes to zero.

Although barotropic instability due to counterpropagating phase-locked VRWs in hurricanes has been studied (Schubert et al. 1999; Kuo et al. 1999; Kossin and Schubert 2001; Reasor and Montgomery 2001; Terwey and Montgomery 2002) while some earlier studies also suggested barotropic instability as the possible cause of tornado subvortices, we are not aware of any published study that performed a detailed analysis of the stability condition of the mean tornado vortex, or the behaviors and characteristics of simulated waves and subvortex propagation. These are performed in this study with a simulation dataset.

The most unstable wavenumber 5 in our simulation is estimated by the method proposed by Schubert et al. (1999) and improved upon by Hendricks et al. (2009) based on a nondivergent 2D barotropic model. The method originally aimed at understanding the asymmetric dynamics of hurricane's eye and eyewall. According to their studies, the end state of asymmetric hurricane eyewall is controlled by the shape of the vorticity ring associated with the hurricane eyewall. Two parameters are used to quantify the structure of the vorticity ring: the thickness parameter, defined as the ratio of the inner and outer radii of the vorticity ring, and hollowness, defined as the ratio of the vorticity in the inner region to that of the area-weighted average of vorticity out to edge of the vorticity ring. Using these two parameters, the growth rates of different wavenumbers and then the most unstable wavenumber can be estimated. The values of these two parameters estimated for the vorticity ring in our simulation, immediately prior to the subvortex formation, correctly indicate that 5 is the most unstable wavenumber, with a growth rate of 0.14. This suggests that the unstable growth of VRWs due to barotropic instability is the cause of the nonlinear development of the subvortices. An analysis on the terms in the perturbation kinetic energy equation further shows that the largest contribution to the perturbation kinetic energy increase is the term associated with radial shear of azimuthal wind, further confirming the barotropic instability is the main mechanism for wave amplification.

As the unstable VRWs grow, the vorticity ring evolves into five isolated subvortices. At the mature stage of subvortices, nonlinear vorticity dynamics play important roles. During the amplification and maintenance stages of the subvortices, vertical stretching is the largest production term of vertical vorticity. Vertical vorticity stretching is mostly positive at the subvortex locations and plays a key role in offsetting vorticity sink by friction and vertical advection so as to intensify and maintain the subvortices for more than 6 min. The vertical

vorticity in the subvortices in the southeastern part of the overall tornado vortex is generally larger during the period that the subvortices are clearly defined and before the establishment of subvortices. This asymmetric vorticity pattern is linked to the wavenumber-1 component of vertical velocity that modulates vertical stretching and possibly also tilting. The wavenumber-1 component of vertical velocity is positive in the southeastern part of the overall tornado vortex, leading to stronger subvortices at those locations. Conversely, the wavenumber-1 component of vertical velocity is negative in the northwestern part of the overall tornado vortex, resulting in an overall weaker vertical stretching and correspondingly weaker subvortices at those locations.

Although the above characteristics share many similarities with tropical cyclones, the isolated subvortices are not as pronounced in tropical cyclones but instead exhibit themselves in the form of polygonal eyewalls. That may be because the relative amounts of energy available for subvortex intensification are different between hurricanes and tornadoes. In tropical cyclones, a significant amount of energy for VRWs is from diabatic heating, which is absent for VRWs in tornadoes. In tornadoes, vertical stretching is the most predominant term in the vorticity equation, providing energy for VRW amplification. The amplitudes of VRWs in tornadoes can grow large enough to form discrete subvortices whose local circulation strength is comparable to the strength of the azimuthal mean circulation. In addition to the more localized stretching mechanism, the absence of diabatic heating associated with tornado VRWs causes the spiral vertical vorticity bands to be relatively weak while spiral rainbands enhanced by diabatic heating (and production of potential vorticity) are prominent features in tropical cyclones (Chen and Yau 2001; Li and Wang 2012; Hall et al. 2013).

Gall (1983) found that for smaller swirl ratios the most unstable wave modes receive most energy from the radial shear of vertical velocity, and only azimuthal wavenumbers 1 and 2 are unstable. For higher swirl ratios, the unstable wave energy is gained from the radial shear of tangential wind and can produce higher wavenumbers that are unstable (i.e., above 4). Recently, Dahl (2021) studied the mechanism responsible for vortex breakdown corresponding to “smaller swirl ratios” in Gall (1983). According to his work, the vortex breakdown phenomenon is analogous to hydraulic jump, except for being related to the Kelvin waves. If the downward-propagating Kelvin wave dominates the upward advection of the waves associated with the environment, the result is a vortex breakdown. Once the vortex breakdown reaches the surface, the two-cell structure (i.e., vorticity ring) forms with downward motion in the vortex interior. The instability energy source in the vortex breakdown stage mainly comes from the radial gradient of vertical velocity (Dahl 2021) or the vertical gradient of vertical velocity (Nolan 2012). Our study fills some theoretical gaps about the formation mechanism of subvortices in tornadoes after the vorticity ring has formed, which corresponds to “higher swirl ratios” in Gall (1983). After the vorticity ring is formed, the formation mechanism of subvortices is attributed to barotropic instability generated by phase-locked counterpropagating VRWs on the inner and outer

sides of the ring. The perturbation energy production at the early stages of VRWs is associated with the radial shear of tangential wind, and further amplification and maintenance of the subvortices are attributed to stretching of vertical vorticity, created mainly by tilting of horizontal vorticity. Although neither the theory of VRWs nor barotropic instability resulting from counterpropagating VRWs is new, the main goal of our paper is not to claim that we have discovered a new mechanism or a new wave model. Our main goal is to demonstrate that unstable VRWs play a primary role in the development of multiple subvortices in a numerically simulated realistic tornado (based on a real case), which we believe may also reflect real-world tornadoes.

We also see that the VRWs can activate IGWs in the stable stratification above. The interaction between VRWs and IGWs is a topic deserving further research, as is the role and effects of positive vertical velocity bands in the outer region of tornado vortex. Our analyses presented in this paper are based on the simulation of a single tornado case. More cases should be examined to test the generality of our conclusions. The lack of subvortex-resolving observations poses challenges to directly study their mechanisms in real tornadoes. [Bluestein et al. \(2003\)](#) and [Tanamachi et al. \(2007\)](#) found using Doppler radar data that the observed subvortices propagated at speeds slower than the maximum mean azimuthal velocity, which is in agreement with the characteristics of VRWs. Both found that wavenumber 2 was the dominant wave but their data could not resolve the fine-scale features of VRWs or subvortices. Such features may also result from the distortion of the vortex due to vortex motion ([Tanamachi et al. 2007](#)). Therefore, more rapid-scan, higher-resolution, volumetric radar data need to be collected to

substantiate the mechanism advanced in this paper from the observational perspective.

Acknowledgments. This work was primarily supported by NSFC Grant 41730965. Zhenqi Sun is acknowledged for making available his simulation configuration and data.

Data availability statement. The data used in this paper can be found at Harvard Dataverse at <https://dataverse.harvard.edu/dataset.xhtml?persistentId=doi:10.7910/DVN/ZG6Y44&version=DRAFT>.

APPENDIX A

Estimation of the Wavelengths of Wavenumbers 1–4

The radial wavelengths of wavenumbers 1–4 are estimated subjectively, the same as wavenumber 5 ([Fig. A1](#)). The distance between maximum and minimum of decomposed vorticity is 1/2 radial wavelength. We measure the radial separation between the maximum and minimum values of vorticity in the time–radius Hovmöller diagram for each azimuthal wavenumber in the plotted graph, and similarly measure the separation between 250 m radial tick marks. Then the ratio between the two separations can be calculated. The radial wavelength is twice the product of this ratio and 250 m. The radial wavelengths of wavenumbers 1–4 are estimated as 250, 229.2, 243.1, and 277.8 m, respectively. Note that the radial structures of wavenumbers 3 and 4 at this time are not well organized, leading to more uncertainties in the estimation of radial wavelengths.

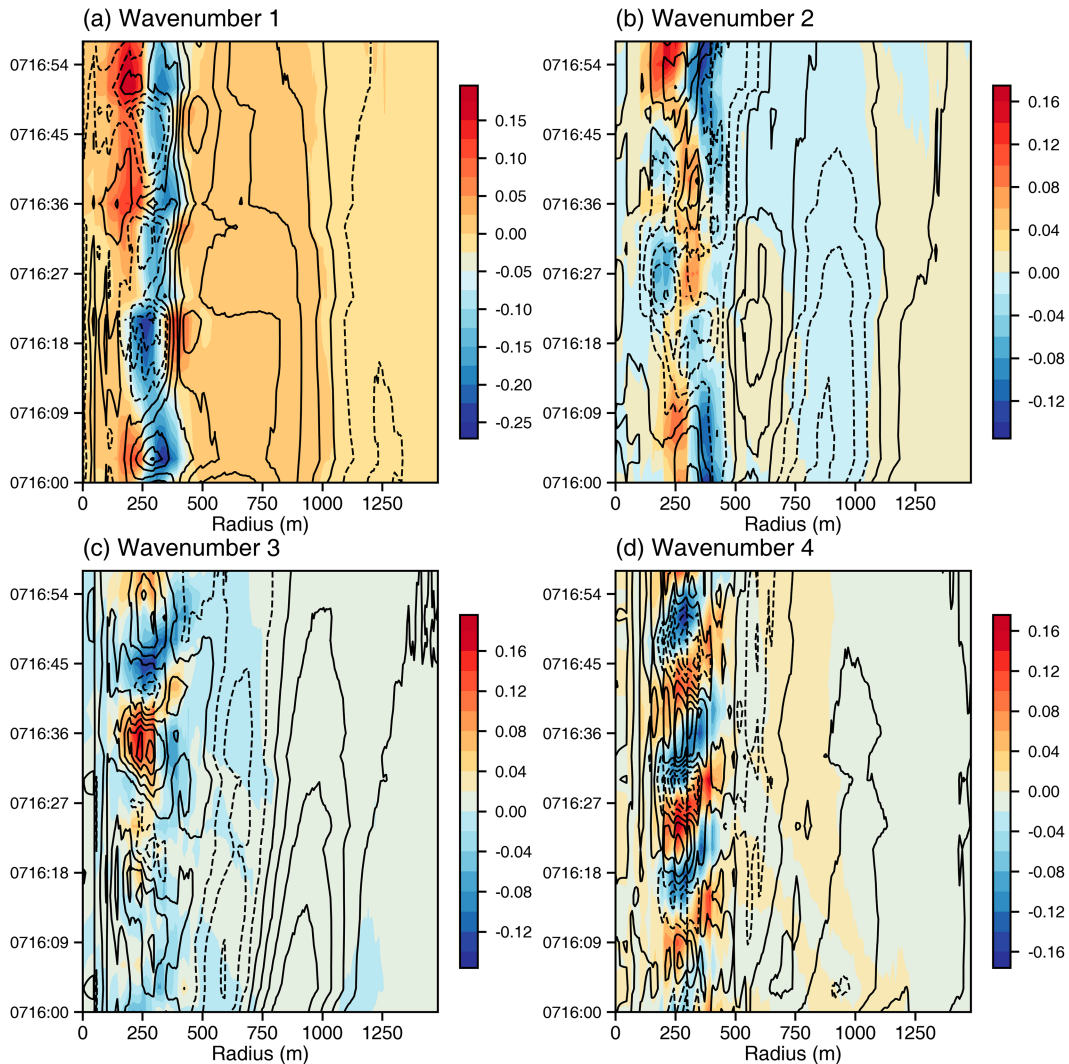


FIG. A1. As in Fig. 5b, but for the time–radius Hovmöller diagram of wavenumber (a) 1, (b) 2, (c) 3, and (d) 4, ζ (shaded; s^{-1}) and w [contour intervals are 3, 1.5, 1.5, and 1.5 $m s^{-1}$ in (a)–(d), respectively; positive solid and negative dashed] from the tornado center to 1500 m south at ~ 26 m AGL from 0716:00 to 0716:57 UTC of time integration.

APPENDIX B

The Characteristics of VRWS at 0724 UTC at ~ 26 m AGL

The parameters of decomposed waves, including azimuthal and radial phase speeds, azimuthal and radial group velocities, and the stagnation radius, are calculated at 0724 UTC at ~ 26 m AGL. The wavelengths of wavenumbers 1–5, estimated using the same method as described in appendix A, are 277.8, 375.0, 277.8, 236.1, and 382.4 m. The corresponding azimuthal phase speeds are 48.6, 43.2, 49.1, 51.2, and 46.2 $m s^{-1}$, respectively. The maximum azimuthal mean tangential wind speed is 55.9 $m s^{-1}$ and is at a radius of 453.2 m. It takes ~ 60 s for the waves to rotate a full circle, and the overall rotation

speed of waves is about 47.5 $m s^{-1}$, consistent with the theoretically estimated azimuthal speed. The azimuthal group velocities of wavenumbers 1–5 are 48.7, 44.9, 50.2, 52.1, and 52.3 $m s^{-1}$, respectively. The radial phase speeds of wavenumbers 1–5 are 4.7, 11.4, 14.4, 17.0, and 31.0 $m s^{-1}$, respectively. The radial group velocities of wavenumbers 1–5 are 1.4, 6.3, 3.7, 2.9, and 9.1 $m s^{-1}$. The stagnation radii of wavenumbers 1–5 are 721.8, 732.0, 721.4, 717.8, and 729.7 m, respectively. The stagnation radii of wavenumbers 1–5 calculated by formula are larger than Fig. B1 shown and the radial phase speed of wavenumber 5 seems unrealistically large; this may be because vorticity dynamics including tilting and stretching are playing significant roles beyond barotropic instability.

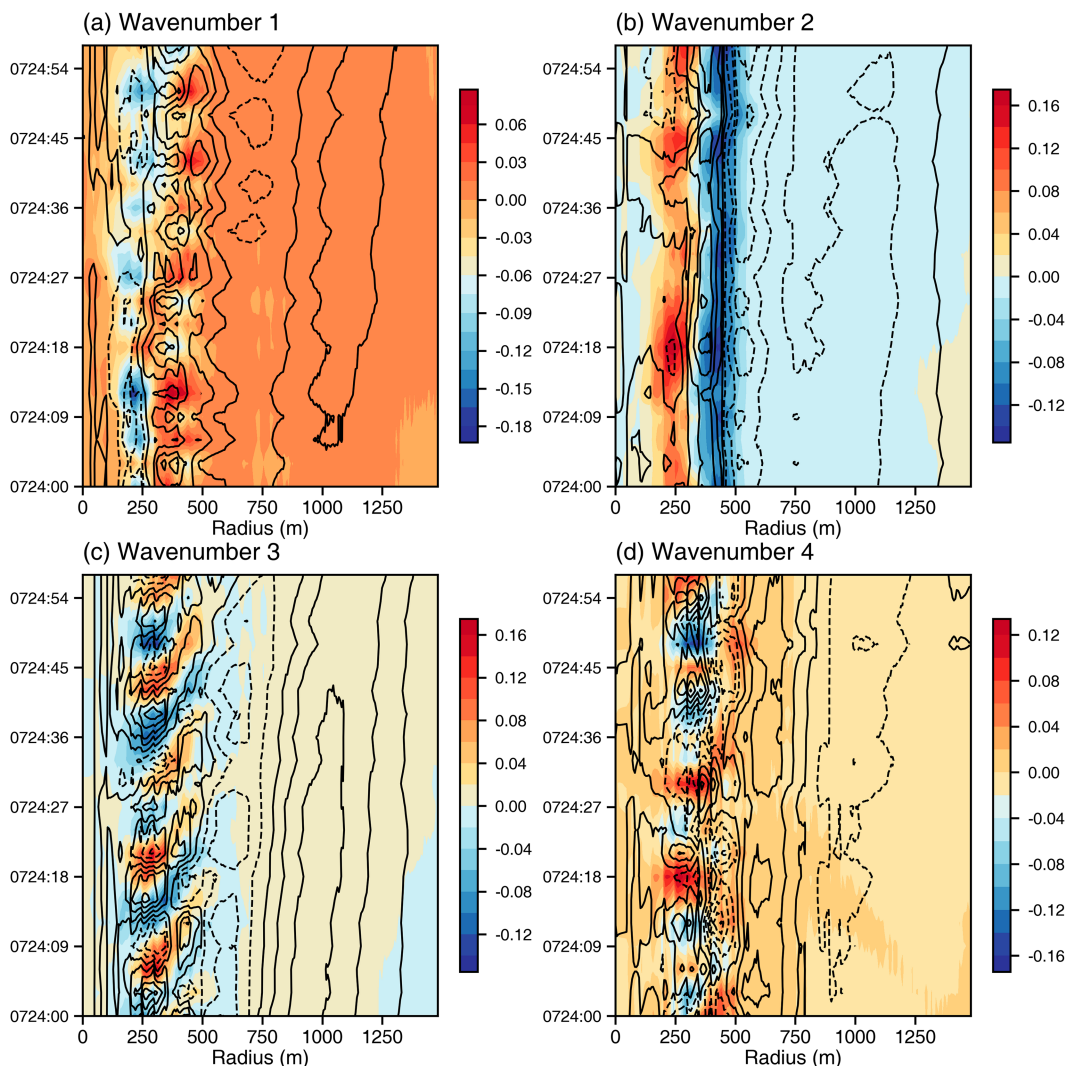


FIG. B1. As in Fig. 5d, but for the time–radius Hovmöller diagrams of wavenumbers (a) 1, (b) 2, (c) 3, and (d) 4, ζ (shaded; s^{-1}) and w [contour intervals are 1.5, 2, 1.5, and 1.5 $m s^{-1}$ in (a)–(d), respectively; positive values are solid and negative dashed] from the tornado center to 1500 m to the south at ~ 26 m AGL from 0724:00 to 0724:57 UTC.

APPENDIX C

The Fourier Decomposition of ζ and W at 0724 UTC at ~ 322 m AGL

Figure C1 is the same as Fig. 6, but for fields at ~ 322 m AGL, a level near the top of the ring of large vorticity (cf. Fig. 10).

For the dominant wavenumber-5 mode, the patterns of ζ and w are similar to those at ~ 26 m in Fig. 6, with the phase at ~ 322 m lagging slightly behind, and magnitude of w is larger and that of ζ is smaller at the higher level. The patterns of other wavenumbers are also generally similar at the two levels, suggesting that the waves are mostly barotropic.

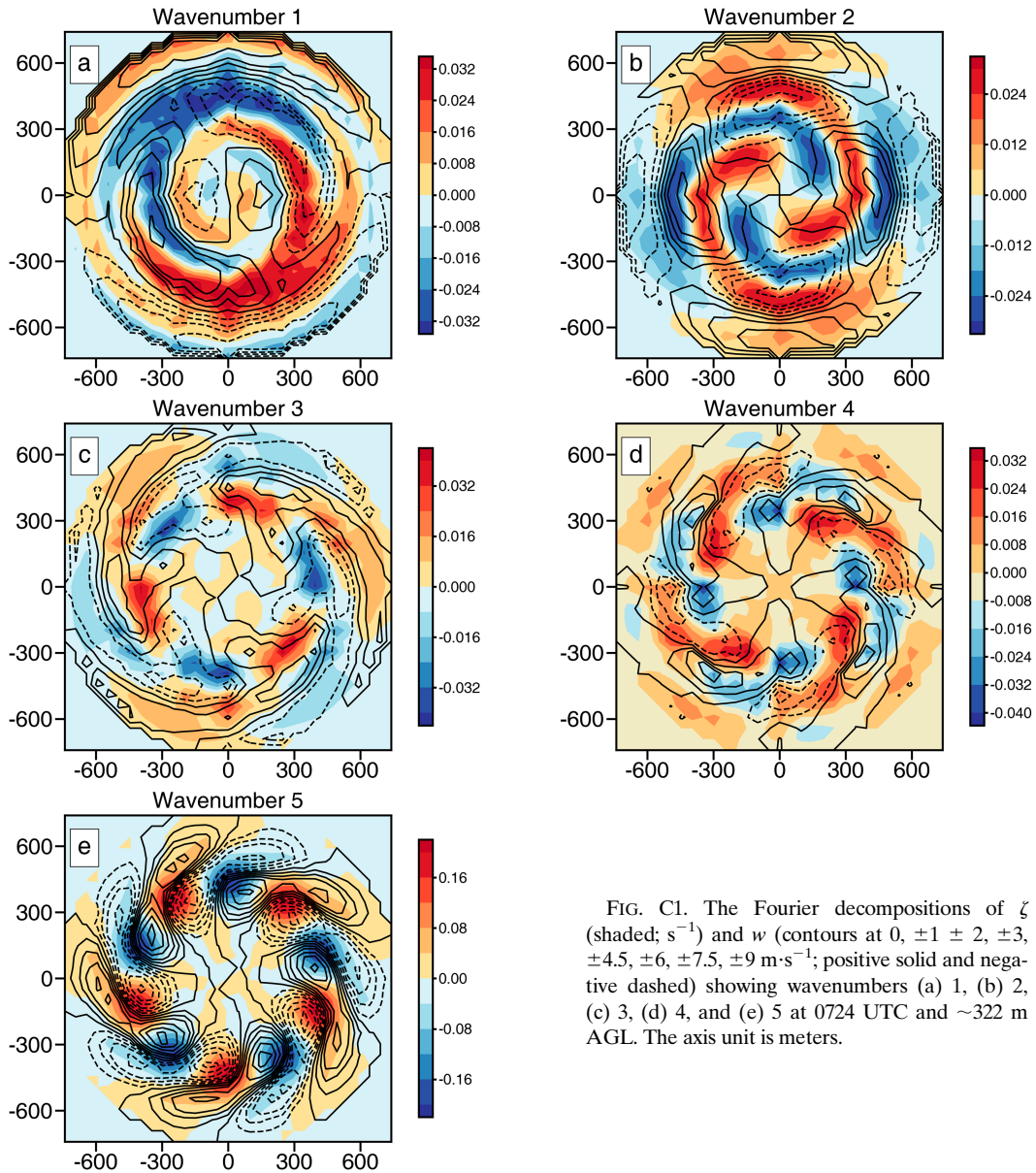


FIG. C1. The Fourier decompositions of ζ (shaded; s^{-1}) and w (contours at $0, \pm 1 \pm 2, \pm 3, \pm 4.5, \pm 6, \pm 7.5, \pm 9 \text{ m}\cdot\text{s}^{-1}$; positive solid and negative dashed) showing wavenumbers (a) 1, (b) 2, (c) 3, (d) 4, and (e) 5 at 0724 UTC and $\sim 322 \text{ m}$ AGL. The axis unit is meters.

REFERENCES

- Alexander, C. R., and J. Wurman, 2005: The 30 May 1998 Spencer, South Dakota, storm. Part I: The structural evolution and environment of the tornadoes. *Mon. Wea. Rev.*, **133**, 72–97, <https://doi.org/10.1175/MWR-2855.1>.
- Bluestein, H. B., W.-C. Lee, M. Bell, C. C. Weiss, and A. L. Pazmany, 2003: Mobile Doppler radar observations of a tornado in a supercell near Bassett, Nebraska, on 5 June 1999. Part II: Tornado-vortex structure. *Mon. Wea. Rev.*, **131**, 2968–2984, [https://doi.org/10.1175/1520-0493\(2003\)131<2968:MDROOA>2.0.CO;2](https://doi.org/10.1175/1520-0493(2003)131<2968:MDROOA>2.0.CO;2).
- Braun, S. A., M. T. Montgomery, and Z. Pu, 2006: High-resolution simulation of Hurricane Bonnie (1998). Part I: The organization of eyewall vertical motion. *J. Atmos. Sci.*, **63**, 19–42, <https://doi.org/10.1175/JAS3598.1>.
- Bryan, G. H., N. A. Dahl, D. S. Nolan, and R. Rotunno, 2017: An eddy injection method for large-eddy simulations of tornado-like vortices. *Mon. Wea. Rev.*, **145**, 1937–1961, <https://doi.org/10.1175/MWR-D-16-0339.1>.
- Chen, Y., and M. K. Yau, 2001: Spiral bands in a simulated hurricane. Part I: Vortex Rossby wave verification. *J. Atmos. Sci.*, **58**, 2128–2145, [https://doi.org/10.1175/1520-0469\(2001\)058<2128:SBIASH>2.0.CO;2](https://doi.org/10.1175/1520-0469(2001)058<2128:SBIASH>2.0.CO;2).
- Church, C. R., J. T. Snow, and E. M. Agee, 1977: Tornado vortex simulation at Purdue University. *Bull. Amer. Meteor. Soc.*, **58**, 900–909, [https://doi.org/10.1175/1520-0477\(1977\)058<0900:TVSAPU>2.0.CO;2](https://doi.org/10.1175/1520-0477(1977)058<0900:TVSAPU>2.0.CO;2).
- , —, G. L. Baker, and E. M. Agee, 1979: Characteristics of tornado-like vortices as a function of swirl ratio: A laboratory investigation. *J. Atmos. Sci.*, **36**, 1755–1776, [https://doi.org/10.1175/1520-0469\(1979\)036<1755:COTLVA>2.0.CO;2](https://doi.org/10.1175/1520-0469(1979)036<1755:COTLVA>2.0.CO;2).

- Dahl, J. M. L., 2021: Centrifugal waves in tornado-like vortices: Kelvin's solutions and their applications to multiple-vortex development and vortex breakdown. *Mon. Wea. Rev.*, **149**, 3173–3216, <https://doi.org/10.1175/MWR-D-20-0426.1>.
- Davies-Jones, R., 1986: Tornado dynamics. *Thunderstorms: A Social and Technological Documentary*, 2nd ed. University of Oklahoma Press, 197–236.
- , R. J. Trapp, and H. B. Bluestein, 2001: Tornadoes and tornadic storms. *Severe Convective Storms, Meteor. Monogr.*, No. 50, Amer. Meteor. Soc., 167–221.
- Deardorff, J. W., 1974: Three-dimensional numerical study of turbulence in an entraining mixed layer. *Bound.-Layer Meteor.*, **7**, 199–226, <https://doi.org/10.1007/BF00227913>.
- Fiedler, B. H., 1994: The thermodynamic speed limit and its violation in axisymmetric numerical simulations of tornado-like vortices. *Atmos.–Ocean*, **32**, 335–359, <https://doi.org/10.1080/07055900.1994.9649501>.
- , 1995: On modelling tornadoes in isolation from the parent storm. *Atmos.–Ocean*, **33**, 501–512, <https://doi.org/10.1080/07055900.1995.9649542>.
- , 1998: Wind-speed limits in numerically simulated tornadoes with suction vortices. *Quart. J. Roy. Meteor. Soc.*, **124**, 2377–2392, <https://doi.org/10.1002/qj.49712455110>.
- , 2009: Suction vortices and spiral breakdown in numerical simulations of tornado-like vortices. *Atmos. Sci. Lett.*, **10**, 109–114, <https://doi.org/10.1002/asl.217>.
- Fujita, T. T., 1970: The Lubbock tornadoes: A study of suction spots. *Weatherwise*, **23**, 161–173, <https://doi.org/10.1080/00431672.1970.9932888>.
- , 1972: Tornadoes in Japan and new evidence. *J. Meteor. Soc. Japan*, **50**, 23.
- , 1981: Tornadoes and downbursts in the context of generalized planetary scales. *J. Atmos. Sci.*, **38**, 1511–1534, [https://doi.org/10.1175/1520-0469\(1981\)038<1511:TADITC>2.0.CO;2](https://doi.org/10.1175/1520-0469(1981)038<1511:TADITC>2.0.CO;2).
- , and H. Grandoso, 1968: Split of a thunderstorm into anticyclonic and cyclonic storms and their motion as determined from numerical model experiments. *J. Atmos. Sci.*, **25**, 416–439, [https://doi.org/10.1175/1520-0469\(1968\)025<0416:SOATIA>2.0.CO;2](https://doi.org/10.1175/1520-0469(1968)025<0416:SOATIA>2.0.CO;2).
- , G. S. Forbes, and T. A. Umenhofer, 1976: Close-up view of 20 March 1976 tornadoes: Sinking cloud tops to suction vortices. *Weatherwise*, **29**, 116–145, <https://doi.org/10.1080/00431672.1976.10544142>.
- Gall, R. L., 1983: A linear analysis of the multiple vortex phenomenon in simulated tornadoes. *J. Atmos. Sci.*, **40**, 2010–2024, [https://doi.org/10.1175/1520-0469\(1983\)040<2010:ALAOTM>2.0.CO;2](https://doi.org/10.1175/1520-0469(1983)040<2010:ALAOTM>2.0.CO;2).
- Guinn, T. A., and W. H. Schubert, 1993: Hurricane spiral bands. *J. Atmos. Sci.*, **50**, 3380–3403, [https://doi.org/10.1175/1520-0469\(1993\)050<3380:HSB>2.0.CO;2](https://doi.org/10.1175/1520-0469(1993)050<3380:HSB>2.0.CO;2).
- Hall, J. D., M. Xue, L. Ran, and L. M. Leslie, 2013: High-resolution modeling of Typhoon Morakot (2009): Vortex Rossby waves and their role in extreme precipitation over Taiwan. *J. Atmos. Sci.*, **70**, 163–186, <https://doi.org/10.1175/JAS-D-11-0338.1>.
- Hendricks, E. A., W. H. Schubert, R. K. Taft, H. Wang, and J. P. Kossin, 2009: Life cycles of hurricane-like vorticity rings. *J. Atmos. Sci.*, **66**, 705–722, <https://doi.org/10.1175/2008JAS2820.1>.
- , B. D. McNoldy, and W. H. Schubert, 2012: Observed inner-core structural variability in Hurricane Dolly (2008). *Mon. Wea. Rev.*, **140**, 4066–4077, <https://doi.org/10.1175/MWR-D-12-00018.1>.
- Kosiba, K., and J. Wurman, 2010: The three-dimensional axisymmetric wind field structure of the Spencer, South Dakota, 1998 tornado. *J. Atmos. Sci.*, **67**, 3074–3083, <https://doi.org/10.1175/2010JAS3416.1>.
- Kossin, J. P., and W. H. Schubert, 2001: Mesovortices, polygonal flow patterns, and rapid pressure falls in hurricane-like vortices. *J. Atmos. Sci.*, **58**, 2196–2209, [https://doi.org/10.1175/1520-0469\(2001\)058<2196:MPFPAR>2.0.CO;2](https://doi.org/10.1175/1520-0469(2001)058<2196:MPFPAR>2.0.CO;2).
- , and —, 2004: Mesovortices in Hurricane Isabel. *Bull. Amer. Meteor. Soc.*, **85**, 151–153, <https://doi.org/10.1175/1520-0477-85.2.143>.
- , B. D. McNoldy, and W. H. Schubert, 2002: Vortical swirls in hurricane eye clouds. *Mon. Wea. Rev.*, **130**, 3144–3149, [https://doi.org/10.1175/1520-0493\(2002\)130<3144:VSIHEC>2.0.CO;2](https://doi.org/10.1175/1520-0493(2002)130<3144:VSIHEC>2.0.CO;2).
- Kuo, H.-C., R. T. Williams, and J.-H. Chen, 1999: A possible mechanism for the eye rotation of Typhoon Herb. *J. Atmos. Sci.*, **56**, 1659–1673, [https://doi.org/10.1175/1520-0469\(1999\)056<1659:APMFTE>2.0.CO;2](https://doi.org/10.1175/1520-0469(1999)056<1659:APMFTE>2.0.CO;2).
- Lamb, H., 1932: *Hydrodynamics*. 6th ed. Dover, 732 pp.
- Lee, W.-C., and J. Wurman, 2005: Diagnosed three-dimensional axisymmetric structure of the Mulhall tornado on 3 May 1999. *J. Atmos. Sci.*, **62**, 2373–2393, <https://doi.org/10.1175/JAS3489.1>.
- Lewellen, D. C., and W. S. Lewellen, 2007a: Near-surface intensification of tornado vortices. *J. Atmos. Sci.*, **64**, 2176–2194, <https://doi.org/10.1175/JAS3965.1>.
- , and —, 2007b: Near-surface vortex intensification through corner flow collapse. *J. Atmos. Sci.*, **64**, 2195–2209, <https://doi.org/10.1175/JAS3966.1>.
- , —, and J. Xia, 2000: The influence of a local swirl ratio on tornado intensification near the surface. *J. Atmos. Sci.*, **57**, 527–544, [https://doi.org/10.1175/1520-0469\(2000\)057<0527:TIOALS>2.0.CO;2](https://doi.org/10.1175/1520-0469(2000)057<0527:TIOALS>2.0.CO;2).
- Lewellen, W. S., D. C. Lewellen, and R. I. Sykes, 1997: Large-eddy simulation of a tornado's interaction with the surface. *J. Atmos. Sci.*, **54**, 581–605, [https://doi.org/10.1175/1520-0469\(1997\)054<0581:LESOAT>2.0.CO;2](https://doi.org/10.1175/1520-0469(1997)054<0581:LESOAT>2.0.CO;2).
- Li, Q., and Y. Wang, 2012: A comparison of inner and outer spiral rainbands in a numerically simulated tropical cyclone. *Mon. Wea. Rev.*, **140**, 2782–2805, <https://doi.org/10.1175/MWR-D-11-00237.1>.
- Li, Y., Y. Lin, and Y. Wang, 2019: A numerical study on the formation and maintenance of a long-lived rainband in Typhoon Longwang (2005). *J. Geophys. Res. Atmos.*, **124**, 10401–10426, <https://doi.org/10.1029/2019JD030600>.
- Markowski, P., and Y. Richardson, 2010: *Mesoscale Meteorology in Midlatitudes*. John Wiley and Sons, 432 pp.
- Mashiko, W., and H. Niino, 2017: Super high-resolution simulation of the 6 May 2012 Tsukuba supercell tornado: Near-surface structure and its evolution. *SOLA*, **13**, 135–139, <https://doi.org/10.2151/sola.2017-025>.
- McWilliams, J. C., L. P. Graves, and M. T. Montgomery, 2003: A formal theory for vortex Rossby waves and vortex evolution. *Geophys. Astrophys. Fluid Dyn.*, **97**, 275–309, <https://doi.org/10.1080/0309192031000108698>.
- Meng, Z., and Coauthors, 2018: The deadliest tornado (EF4) in the past 40 years in China. *Wea. Forecasting*, **33**, 693–713, <https://doi.org/10.1175/WAF-D-17-0085.1>.
- Michalke, A., and A. Timme, 1967: On the inviscid instability of certain two-dimensional vortex-type flows. *J. Fluid Mech.*, **29**, 647–666, <https://doi.org/10.1017/S0022112067001090>.
- Möller, J. D., and M. T. Montgomery, 1999: Vortex Rossby waves and hurricane intensification in a barotropic model. *J. Atmos. Sci.*, **56**, 1674–1687, [https://doi.org/10.1175/1520-0469\(1999\)056<1674:VRWAHI>2.0.CO;2](https://doi.org/10.1175/1520-0469(1999)056<1674:VRWAHI>2.0.CO;2).

- , and —, 2000: Tropical cyclone evolution via potential vorticity anomalies in a three-dimensional balance model. *J. Atmos. Sci.*, **57**, 3366–3387, [https://doi.org/10.1175/1520-0469\(2000\)057<3366:TCEVPV>2.0.CO;2](https://doi.org/10.1175/1520-0469(2000)057<3366:TCEVPV>2.0.CO;2).
- Montgomery, M. T., and L. J. Shapiro, 1995: Generalized Charney–Stern and Fjortoft theorems for rapidly rotating vortices. *J. Atmos. Sci.*, **52**, 1829–1833, [https://doi.org/10.1175/1520-0469\(1995\)052<1829:GCAFTF>2.0.CO;2](https://doi.org/10.1175/1520-0469(1995)052<1829:GCAFTF>2.0.CO;2).
- , and R. J. Kallenbach, 1997: A theory for vortex Rossby-waves and its application to spiral bands and intensity changes in hurricanes. *Quart. J. Roy. Meteor. Soc.*, **123**, 435–465, <https://doi.org/10.1002/qj.49712353810>.
- , V. A. Vladimirov, and P. V. Denissenko, 2002: An experimental study on hurricane mesovortices. *J. Fluid Mech.*, **471**, 1–32, <https://doi.org/10.1017/S0022112002001647>.
- Morrison, H., and W. W. Grabowski, 2008: Modeling supersaturation and subgrid-scale mixing with two-moment bulk warm microphysics. *J. Atmos. Sci.*, **65**, 792–812, <https://doi.org/10.1175/2007JAS2374.1>.
- Muramatsu, T., 1986: The structure of polygonal eye of a typhoon. *J. Meteor. Soc. Japan*, **64**, 913–921, https://doi.org/10.2151/jmsj1965.64.6_913.
- Nolan, D. S., 2005: Instabilities in hurricane-like boundary layers. *Dyn. Atmos. Oceans*, **40**, 209–236, <https://doi.org/10.1016/j.dynatmoce.2005.03.002>.
- , 2012: Three-dimensional instabilities in tornado-like vortices with secondary circulations. *J. Fluid Mech.*, **711**, 61–100, <https://doi.org/10.1017/jfm.2012.369>.
- , N. A. Dahl, G. H. Bryan, and R. Rotunno, 2017: Tornado vortex structure, intensity, and surface wind gusts in large-eddy simulations with fully developed turbulence. *J. Atmos. Sci.*, **74**, 1573–1597, <https://doi.org/10.1175/JAS-D-16-0258.1>.
- Pleim, J. E., 2006: A simple, efficient solution of flux–profile relationships in the atmospheric surface layer. *J. Appl. Meteor. Climatol.*, **45**, 341–347, <https://doi.org/10.1175/JAM2339.1>.
- , 2007: A combined local and nonlocal closure model for the atmospheric boundary layer. Part I: Model description and testing. *J. Appl. Meteor. Climatol.*, **46**, 1383–1395, <https://doi.org/10.1175/JAM2539.1>.
- Qiu, X., Z.-M. Tan, and Q. Xiao, 2010: The roles of vortex Rossby waves in hurricane secondary eyewall formation. *Mon. Wea. Rev.*, **138**, 2092–2109, <https://doi.org/10.1175/2010MWR3161.1>.
- Reasor, P. D., and M. T. Montgomery, 2001: Three-dimensional alignment and corotation of weak, TC-like vortices via linear vortex Rossby waves. *J. Atmos. Sci.*, **58**, 2306–2330, [https://doi.org/10.1175/1520-0469\(2001\)058<2306:TDAACO>2.0.CO;2](https://doi.org/10.1175/1520-0469(2001)058<2306:TDAACO>2.0.CO;2).
- , —, F. D. Marks Jr., and J. F. Gamache, 2000: Low-wavenumber structure and evolution of the hurricane inner core observed by airborne dual-Doppler radar. *Mon. Wea. Rev.*, **128**, 1653–1680, [https://doi.org/10.1175/1520-0493\(2000\)128<1653:LWSAEO>2.0.CO;2](https://doi.org/10.1175/1520-0493(2000)128<1653:LWSAEO>2.0.CO;2).
- Roberts, B., and M. Xue, 2017: The role of surface drag in mesocyclone intensification leading to tornadogenesis within an idealized supercell simulation. *J. Atmos. Sci.*, **74**, 3055–3077, <https://doi.org/10.1175/JAS-D-16-0364.1>.
- , —, A. D. Schenkman, and D. T. Dawson II, 2016: The role of surface drag in tornadogenesis within an idealized supercell simulation. *J. Atmos. Sci.*, **73**, 3371–3395, <https://doi.org/10.1175/JAS-D-15-0332.1>.
- , —, and D. T. Dawson II, 2020: The effect of surface drag strength on mesocyclone intensification and tornadogenesis in idealized supercell simulations. *J. Atmos. Sci.*, **77**, 1699–1721, <https://doi.org/10.1175/JAS-D-19-0109.1>.
- Rotunno, R., 1977: Numerical simulation of a laboratory vortex. *J. Atmos. Sci.*, **34**, 1942–1956, [https://doi.org/10.1175/1520-0469\(1977\)034<1942:NSOALV>2.0.CO;2](https://doi.org/10.1175/1520-0469(1977)034<1942:NSOALV>2.0.CO;2).
- , 1978: A note on the stability of a cylindrical vortex sheet. *J. Fluid Mech.*, **87**, 761–771, <https://doi.org/10.1017/S0022112078001871>.
- , 1979: A study in tornado-like vortex dynamics. *J. Atmos. Sci.*, **36**, 140–155, [https://doi.org/10.1175/1520-0469\(1979\)036<0140:ASITLV>2.0.CO;2](https://doi.org/10.1175/1520-0469(1979)036<0140:ASITLV>2.0.CO;2).
- , 1984: An investigation of a three-dimensional asymmetric vortex. *J. Atmos. Sci.*, **41**, 283–298, [https://doi.org/10.1175/1520-0469\(1984\)041<0283:AIOATD>2.0.CO;2](https://doi.org/10.1175/1520-0469(1984)041<0283:AIOATD>2.0.CO;2).
- , G. H. Bryan, D. S. Nolan, and N. A. Dahl, 2016: Axisymmetric tornado simulations at high Reynolds number. *J. Atmos. Sci.*, **73**, 3843–3854, <https://doi.org/10.1175/JAS-D-16-0038.1>.
- Rozoff, C. M., W. H. Schubert, B. D. McNoldy, and J. P. Kossin, 2006: Rapid filamentation zones in intense tropical cyclones. *J. Atmos. Sci.*, **63**, 325–340, <https://doi.org/10.1175/JAS3595.1>.
- Schecter, D. A., and M. T. Montgomery, 2007: Waves in a cloudy vortex. *J. Atmos. Sci.*, **64**, 314–337, <https://doi.org/10.1175/JAS3849.1>.
- Schenkman, A. D., M. Xue, and M. Hu, 2014: Tornadogenesis in a high-resolution simulation of the 8 May 2003 Oklahoma City supercell. *J. Atmos. Sci.*, **71**, 130–154, <https://doi.org/10.1175/JAS-D-13-073.1>.
- Schubert, W. H., M. T. Montgomery, R. K. Taft, T. A. Guinn, S. R. Fulton, J. P. Kossin, and J. P. Edwards, 1999: Polygonal eyewalls, asymmetric eye contraction, and potential vorticity mixing in hurricanes. *J. Atmos. Sci.*, **56**, 1197–1223, [https://doi.org/10.1175/1520-0469\(1999\)056<1197:PEAECA>2.0.CO;2](https://doi.org/10.1175/1520-0469(1999)056<1197:PEAECA>2.0.CO;2).
- Skamarock, W. C., and Coauthors, 2008: A description of the Advanced Research WRF version 3. NCAR Tech. Note NCAR/TN-475+STR, 113 pp., <https://doi.org/10.5065/D68S4MVH>.
- Smagorinsky, J., 1963: General circulation experiments with the primitive equations: I. The basic experiment. *Mon. Wea. Rev.*, **91**, 99–164, [https://doi.org/10.1175/1520-0493\(1963\)091<0099:GCEWTP>2.3.CO;2](https://doi.org/10.1175/1520-0493(1963)091<0099:GCEWTP>2.3.CO;2).
- Snow, J. T., 1978: On inertial instability as related to the multiple-vortex phenomenon. *J. Atmos. Sci.*, **35**, 1660–1677, [https://doi.org/10.1175/1520-0469\(1978\)035<1660:OIHART>2.0.CO;2](https://doi.org/10.1175/1520-0469(1978)035<1660:OIHART>2.0.CO;2).
- Staley, D. O., and R. L. Gall, 1979: Barotropic instability in a tornado vortex. *J. Atmos. Sci.*, **36**, 973–981, [https://doi.org/10.1175/1520-0469\(1979\)036<0973:BIATV>2.0.CO;2](https://doi.org/10.1175/1520-0469(1979)036<0973:BIATV>2.0.CO;2).
- Sun, Z., M. Xue, K. Zhu, and B. Zhou, 2019: Prediction of an EF4 supercell tornado in Funing, China: Resolution dependency of simulated tornadoes and their structures. *Atmos. Res.*, **229**, 175–189, <https://doi.org/10.1016/j.atmosres.2019.06.019>.
- Tanamachi, R. L., H. B. Bluestein, W.-C. Lee, M. Bell, and A. Pazmany, 2007: Ground-based velocity track display (GBVTD) analysis of W-band Doppler radar data in a tornado near Stockton, Kansas, on 15 May 1999. *Mon. Wea. Rev.*, **135**, 783–800, <https://doi.org/10.1175/MWR3325.1>.
- Tao, T., and T. Tamura, 2020: Numerical study of the 6 May 2012 Tsukuba supercell tornado: Vorticity sources responsible for tornadogenesis. *Mon. Wea. Rev.*, **148**, 1205–1228, <https://doi.org/10.1175/MWR-D-19-0095.1>.
- Terwey, W. D., and M. T. Montgomery, 2002: Wavenumber-2 and wavenumber-*m* vortex Rossby wave instabilities in a generalized three-region model. *J. Atmos. Sci.*, **59**, 2421–2427, [https://doi.org/10.1175/1520-0469\(2002\)059<2421:WAWMVR>2.0.CO;2](https://doi.org/10.1175/1520-0469(2002)059<2421:WAWMVR>2.0.CO;2).

- Thomson, W., 1880: Vibrations of a columnar vortex. *London Edinburgh Dublin Philos. Mag. J. Sci.*, **10**, 155–168, <https://doi.org/10.1080/14786448008626912>.
- Walko, R., and R. Gall, 1984: A two-dimensional linear stability analysis of the multiple vortex phenomenon. *J. Atmos. Sci.*, **41**, 3456–3471, [https://doi.org/10.1175/1520-0469\(1984\)041<3456:ATDLSA>2.0.CO;2](https://doi.org/10.1175/1520-0469(1984)041<3456:ATDLSA>2.0.CO;2).
- Wang, Y., 2002: Vortex Rossby waves in a numerically simulated tropical cyclone. Part II: The role in tropical cyclone structure and intensity changes. *J. Atmos. Sci.*, **59**, 1239–1262, [https://doi.org/10.1175/1520-0469\(2002\)059<1239:VRWIAN>2.0.CO;2](https://doi.org/10.1175/1520-0469(2002)059<1239:VRWIAN>2.0.CO;2).
- Ward, N. B., 1972: The exploration of certain features of tornado dynamics using a laboratory model. *J. Atmos. Sci.*, **29**, 1194–1204, [https://doi.org/10.1175/1520-0469\(1972\)029<1194:TEOCFO>2.0.CO;2](https://doi.org/10.1175/1520-0469(1972)029<1194:TEOCFO>2.0.CO;2).
- Wurman, J., 2002: The multiple-vortex structure of a tornado. *Wea. Forecasting*, **17**, 473–505, [https://doi.org/10.1175/1520-0434\(2002\)017<0473:TMVSOA>2.0.CO;2](https://doi.org/10.1175/1520-0434(2002)017<0473:TMVSOA>2.0.CO;2).
- Xue, M., M. Hu, and A. D. Schenkman, 2014: Numerical prediction of the 8 May 2003 Oklahoma City tornadic supercell and embedded tornado using ARPS with the assimilation of WSR-88D data. *Wea. Forecasting*, **29**, 39–62, <https://doi.org/10.1175/WAF-D-13-00029.1>.
- , K. Zhao, M. Wang, Z. Li, and Y. Zheng, 2016: Recent significant tornadoes in China. *Adv. Atmos. Sci.*, **33**, 1209–1217, <https://doi.org/10.1007/s00376-016-6005-2>.